Kr-Ar LASER RAMAN SPECTROMETER FOR LOW TEMPERATURE MEASUREMENTS

by

Graeme M. Wardlaw

B. Sc. (Mathematics and Physics), Brock University

A THESIS SUBMITTED IN PARTIAL FULFILMENT OF
THE REQUIREMENTS FOR THE DEGREE OF

MASTER OF SCIENCE

in

Faculty of Mathematics and Science

Department of Physics

BROCK UNIVERSITY

September 1, 2004

2004 © Graeme M. Wardlaw

In presenting this thesis in partial fulfilment of the requirements for an advanced degree at the Brock University, I agree that the Library shall make it freely available for reference and study. I further agree that permission for extensive copying of this thesis for scholarly purposes may be granted by the head of my department or by his or her representatives. It is understood that copying or publication of this thesis for financial gain shall not be allowed without my written permission.

(Signature) _____

Department of Physics

Brock University
St.Catharines, Canada

Date _____

Abstract

A Czerny Mount double monochromator is used to measure Raman scattered radiation near 90° from a crystalline, Silicon sample. Incident light is provided by a mixed gas Kr-Ar laser, operating at 5145 Å. The double monochromator is calibrated to true wavelength by comparison of Kr and Ar emission line positions (Å) to grating position (Å) display [1]. The relationship was found to be linear and can be described by,

$$y = 1.219873x - 1209.32, \tag{1}$$

where y is true wavelength (Å) and x is grating position display (Å). The Raman emission spectra are collected via C^{++} encoded software, which displays a mV signal from a Photodetector and allows stepping control of the gratings via an A/D interface. [2]

The software collection parameters, detector temperature and optics are optimised to yield the best quality spectra. The inclusion of a cryostat allows for temperature dependent capability ranging from 4 K to $\approx$ 350 K.

Silicon Stokes temperature dependent Raman spectra, generally show agreement with literature results [3] in their frequency hardening, FWHM reduction and intensity increase as temperature is reduced. Tests reveal that a re-alignment of the double monochromator is necessary before spectral resolution can approach literature standard. This has not yet been carried out due to time constraints.

Contents

List of Tables

List of Figures

Acknowledgements

My appreciation to Dr. M. Reedyk who assisted and supervised this project. I was fortunate enough to continue working with her after also completing my undergraduate thesis, which was later published. I have learned much more as I continued on under her supervision.

Of course, this being a "building" thesis I could not have completed much without the help of Roland, Art, Steve and the apprentices in the machine shop. They were always willing to help even when the physics department had them snowed under with more projects than they could handle. They did a fantastic job.

Many thanks to Dr. S. Bose and Dr. F. Razavi for sitting on my supervisory panel and answering questions as I worked towards finishing. As well, Dr. D. Crandles for answering the many questions over the last two years. And my thanks to Dr. E. Sternin for all of his help with Latex and the UNIX workstations.

I also owe a great deal of gratitude to Dr. R. Hackl on his visit to Brock University. Not only did he give a stimulating talk, he was kind enough to tour our lab and provide some expert opinion and direction.

Of course last, but not least I owe many, many thanks to Sudhakar and my peers for helping along the way. Various points of stress, confusion and anxiety were diffused through many helpful conversations. Rob, Mehdi, Amir, Avid, Stan, Suzana, Ivana, Henrich, Taleyeh, Helia, and Roshanak. As well as Mike, Gerry, Andrew and the rest of the B 203 club.

Finally, thanks to Rebecca for initiating my masters application, immense support and seeing me through.

Chapter 1

Introduction

The field of spectroscopy is vast and intensive. Many different techniques give rise to a wide array of tools to be used in investigating the properties of various materials. In this work, our main interest is in vibrational spectroscopy: where vibrations are caused by the sample molecule absorbing a particular discrete amount of energy from the illuminating radiation. Two major fields of vibrational Spectroscopy exist and are commonly employed; Infrared and Raman. Both are rich in terms of the information they can provide, but are distinctly complimentary (See Table 1.1) even though they operate within similar frequency ranges. Selection rules that exist for Infrared (IR) transitions may be forbidden in the Raman scheme and vice versa. Consequently, an arrangement of both systems working in tandem may prove to be a more powerful diagnostic tool than one system alone [4], [5]. Hence, the underlying motivation behind this project was to

	RAMAN	INFRARED
Incident Frequency	Maintained	Varied continuously
Vibrations	Polarisability	Change in dipole moment
Range	MIR–FIR ($4000\text{-}50$ cm^{-1})	NIR–FIR ($13\,300$ - 50cm^{-1})
Band (Peak) Type	Emission	Absorption

Table 1.1: Spectroscopy Comparison: Raman vs. Infrared.

provide a system for reliable, high quality Raman spectroscopic measurements to be used in conjunction with the existing Infrared Spectroscopy facilities. The Infrared apparatus consisted of a Martin-Puplett type polarising Interferometer and a Bruker wide range Michelson Interferometer.

In working towards this goal, several inherent problems in the *Jarrel Ash 25-100*
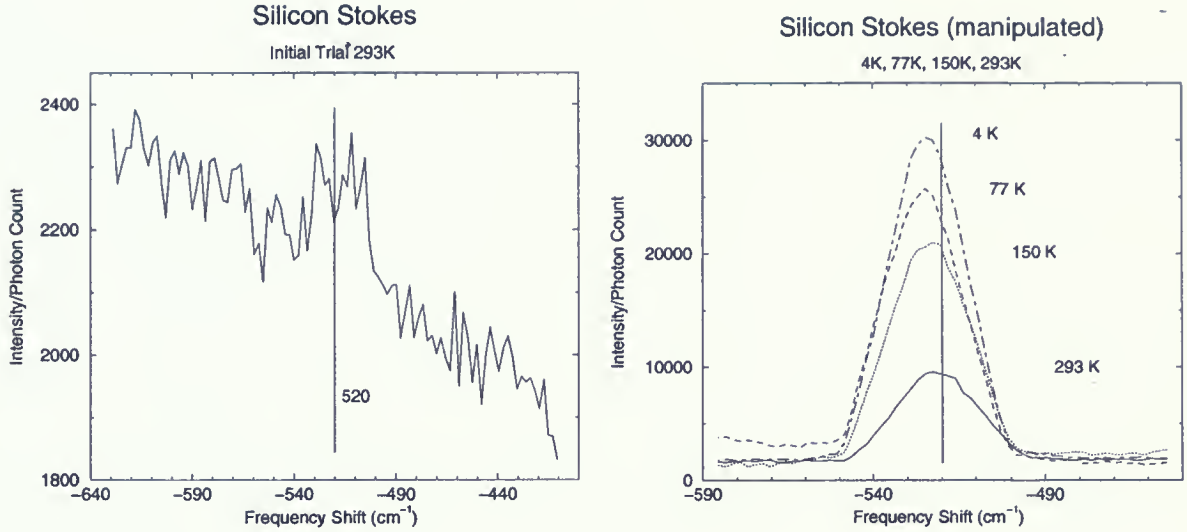
Figure 1.1: Overall Effect of Work Completed. Collection times per data point are 10.0s (1.00s, 10 readings) and 76.5s (2.55s, 30 readings) respectively.

Czerny-Turner double monochromator system were revealed and investigated further to allow the best possible settings and experimental procedure to be found. Many aspects of the system had to be investigated, including: sample mounting, optics arrangement, including incorporation of a cryostat for low temperature measurements, system calibration, software collection settings and detector temperature optimisation. After completion, a significant improvement in spectral quality was observed. This is demonstrated by Figure 1.1 which shows the first scan of the 1st order Silicon TO phonon mode taken compared with one of the last after work was completed. (The initial trial is also shown later in Figure 4.6 in terms of Monochromator Wavelength.) Clearly, vast improvement was made on noise reduction, signal strength and resolution. Also, the overall decreasing (or rising in terms of wavelength) structure seen in the first graph is eliminated in the second, giving a typical flat background and well defined phonon peak.

At the outset of this project, software had been written by [2] to control the movement of the gratings and collect the signal counted by a newly installed photodetector. Prior to this, some preliminary work was done to set up and characterise the emission lines

of the Kr/Ar mixed gas laser and to adjust the spectrometer to scan within the range accessible to Raman Stokes spectra using lines from this laser [6]. Although, both of these previous projects culminated in an attempt to obtain a Raman scattering spectrum from crystalline Silicon, neither succeeded.

The work completed for this thesis is presented quasi-chronologically to try to provide some sense of progression and overall improvement. Thus, some discussion may be briefly outlined and continued later in other dedicated chapters. Chapter 2 begins with some basic Raman Theory to provide a "flavour" of the physics involved. The theory focuses on 1st order Raman Scattering since, as alluded to above, the 1st Transverse Optical phonon mode for Silicon has been extensively studied in the literature. The reader is encouraged to refer to the citations given for more detailed information. Chapters 3 and 4 outline the instrumentation and experimental methods utilised and include a description of the method used to calibrate the spectrometer. These chapters also include descriptions of the original collection optics and sample mounting procedures that were consequently changed to new arrangements. Following this is a presentation and discussion of several diagnostic tests, including the effects of changing software collection parameters and detector cooling system settings in chapters 5 and 6 respectively. Chapter 7 presents a description of the slit optimisation procedure and preliminary Silicon Stokes room temperature spectra. From these results it became clear that a re-alignment of the internal spectrometer optics is necessary before high resolution spectra can be obtained. Chapter 8 presents Silicon Stokes temperature dependent data and includes some discussion and comparison to literature. Finally, Chapter 9 includes a brief discussion of the results and outlines some possible considerations to further improve the quality of the Raman spectra obtained by the system.

Chapter 2

Theory of Raman Scattering

2.1   Overview

Raman Scattering is concerned with the interaction of photons with matter. Like any classical kinematics problem, the two interacting particles may yield an elastic or inelastic collision. Classically, an **elastically scattered** object in a collision with an infinitely massive object emerges with no gain or loss in energy, while an **inelastically scattered** object gains or loses some energy in the process. Photons interacting with electrons may also be scattered elastically or inelastically. Elastically scattered photons are termed Rayleigh scatter, while inelastically scattered photons are considered as Raman scatter [5], after C. V. Raman who won the Nobel prize in 1928 for his work. [7]

In elastically scattered light, incident photons cause electrons in the sample molecule to be temporarily excited to a higher energy state. These electrons then decay back to their original state, releasing a photon of the same incident frequency (see Figure 2.1). The energy of the incident photon is the same as the scattered photon and is given as;

$$E_o = \hbar \omega_o \qquad (2.1)$$

Here, ω_o represents the incident laser frequency. The interacting photon has neither lost nor gained energy, hence is scattered elastically. In most cases, Rayleigh scattering makes up only approximately 10^{-3} - 10^{-5} [5] of the incident radiation, whereas Raman is much smaller than this again, comprising only 10^{-6} - 10^{-7} of the incident radiation [8], [9].

In Raman scattering the process is very similar to Rayleigh scattering. However, in this
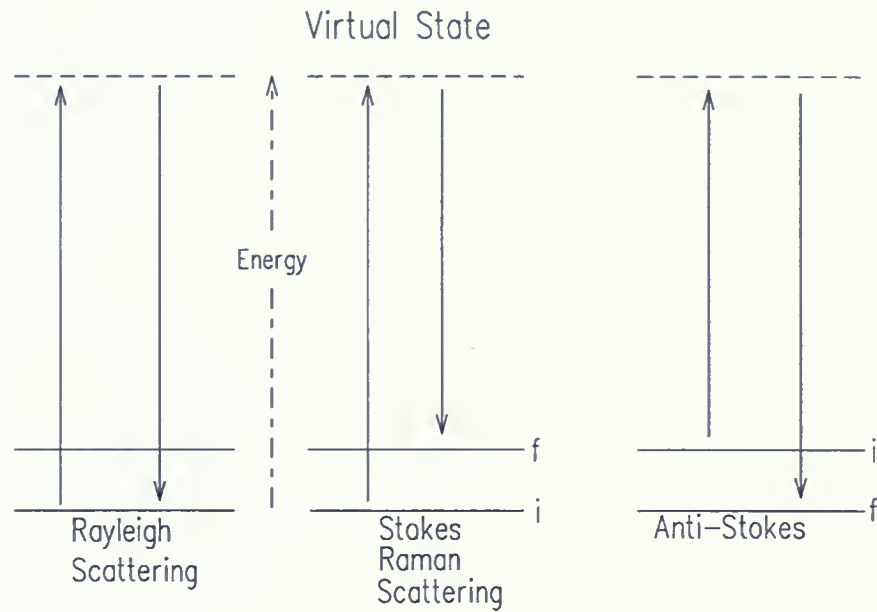
Figure 2.1: The Scattering Processes.
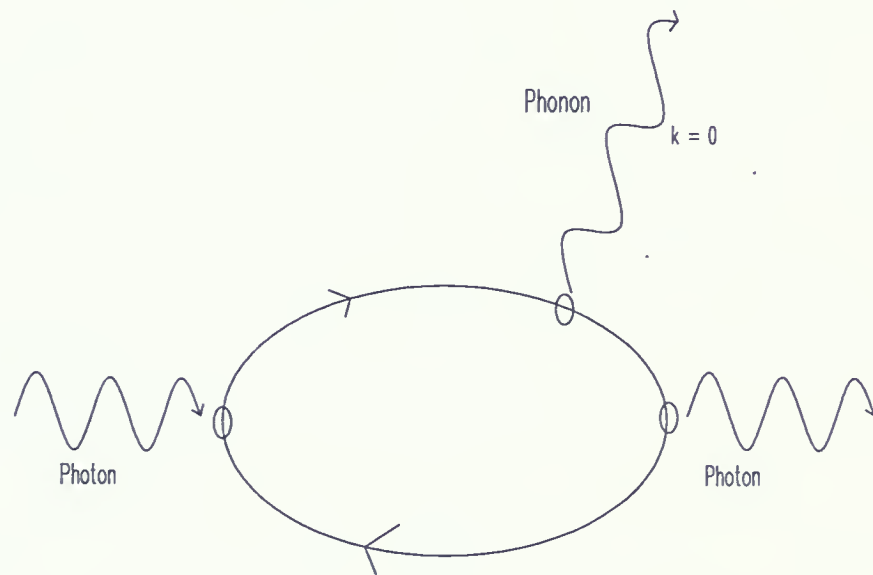
Figure 2.2: Photon and Electron Interaction.

case the excited electron does not decay to its original state. Instead, it decays to a state above or below its original state. This implies that the photon released as the electron decays, is either of lower or greater energy than the incident photon. Since frequency is proportional to energy we may write the scattered photon energies as;

$$E_o = \hbar(\omega_o \pm \omega_i). \tag{2.2}$$

So as we see, the raman scattered terms are given as functions of **shift**, ω_i, from the incident frequency, ω_o. Figure 2.1 describes the two possible Raman scattering cases, commonly referred to as **Stokes** and **Anti-Stokes** radiation. In Stokes Raman scattering, the electron decays back to a state above its original state, releasing a photon of lower energy and frequency $(\omega_o - \omega_i)$ than the incident. For Anti-Stokes scattering the photon emitted is of higher energy and frequency $(\omega_o + \omega_i)$ than the incident photon. This implies that in a frequency dependent Raman spectrum, Stokes lines occupy the region to the left of the incident laser line and Anti-Stokes to the right [5].

In **phonon Raman Scattering**, the frequency component ω_i is representative of the phonon frequency involved in the scattering event. During the Stokes process the incident photon (ω_0) interacts with the lattice to create a phonon (ω_i) and scattered photon $(\omega_0 - \omega_i)$, while during the Anti-Stokes process the incident photon (ω_0) and a thermal phonon (ω_i) interact to create the scattered photon $(\omega_0 + \omega_i)$, essentially annihilating the original thermal phonon. (See Figure 2.2). If the phonon population is initially in thermal equilibrium at some temperature T, then the intensity ratio of the Stokes to Anti-Stokes lines can be summarised as follows;

$$\frac{I(\omega_0 + \omega_i)}{I(\omega_0 - \omega_i)} = e^{\frac{-\hbar\omega_i}{k_B T}}. \tag{2.3}$$

As temperature approaches absolute zero, the relative intensity of the Anti-Stokes line vanishes since there are no thermal phonons available to be annihilated. Eqn. 2.3 also

serves as a means to approximate the temperature of the sample. One simply obtains a ratio of the Stokes intensity to Anti-Stokes and by utilising the Boltzmann and Planck constants with the given shift ω_i, the corresponding sample temperature follows [10].

2.2   Induced Dipole Moment and Polarisability

Absorption of infrared radiation occurs only when there is a change in the dipole moment of the molecule during a normal vibration. To be Raman active, the molecular vibration must include a change in **induced dipole moment**. This implies a change in the **polarisability** of the molecule. For example, consider an electron cloud placed between two charged plates. The field between the plates forces a separation of charge and distortion in the electron cloud. Changing the polarity of the plates causes a change in the opposite direction. By switching polarity at a given frequency, we create a vibrating, induced dipole. Similarly, light used in Raman experiments induces a vibrating dipole in the sample molecule, at the same frequency of the incident radiation. Invoking the notation for the incident frequency used in sect. 2.1, we could write the oscillating field from the laser as [9];

$$\epsilon = \epsilon_o cos(\omega_o t + \delta), \tag{2.4}$$

where ϵ_o is the incident field amplitude, ω_o represents the incident frequency and δ is a phase term.

In classical terms, the scattered radiation is emitted by the vibrating dipole in the form of electromagnetic waves. The intensity of this radiation depends on the polarisability of the molecule and the polarisability of the molecule is dependent upon the displacements of the electrons under the influence of the oscillating field from the incident radiation.

Consequently, the induced dipole moment, μ, can be written as,

$$\mu = \alpha\epsilon, \tag{2.5}$$

where α is polarisability and ϵ represents electric field. Of course, since μ and ϵ are vectors, the polarisability may be written in terms of a **polarisability tensor**, given by a system of 3 coupled equations:

$$\mu_x = \alpha_{xx}E_x + \alpha_{xy}E_y + \alpha_{xz}E_z \tag{2.6}$$

$$\mu_y = \alpha_{yx}E_x + \alpha_{yy}E_y + \alpha_{yz}E_z \tag{2.7}$$

$$\mu_z = \alpha_{zx}E_x + \alpha_{zy}E_y + \alpha_{zz}E_z. \tag{2.8}$$

The polarisability tensor has six unique components [9]. If any one of the six change, the mode is considered Raman active. In other words, a transition is considered Raman Active if the polarisability of the molecule changes during the vibrations [11].

Generally, the polarisability tensor is symmetric, implying that off-diagonal components are equal:

$$\alpha_{xy} = \alpha_{yx} \tag{2.9}$$

$$\alpha_{yz} = \alpha_{zy} \tag{2.10}$$

$$\alpha_{xz} = \alpha_{zx}. \tag{2.11}$$

This fact may then be used to further simplify the tensor [9].

Chapter 3

Instrumentation

This chapter includes a description of the instrumentation used to measure emission spectra of crystalline Silicon. The chapter opens with an overview of the double monochromator, laser source and detector. A discussion of different optical arrangements (original and modified) and computer software follows.

3.1   Double Monochromator

The monochromator used is a *Jarrel-Ash 25-100 Double Czerny-Turner* mount scanning spectrometer. The gratings used are 1180 lines/mm ruled on a 102 mm by 102 mm slab. The spectrometer has a focal length of 1.0 m [12].

The double monochromator has a standard layout. Light is passed through an entrance slit entering the first monochromator and is dispersed by the first grating. The dispersed light then passes through an intermediate slit to a second monchromator where it is dispersed a second time before being directed toward the exit slit and photodetector, as shown in Figure 3.1. Consequently, we obtain light that is spatially separated into frequency components and the exit slit serves to "select" a narrow band of the spectrum for incidence on the photodetector. Any light of the incident laser frequency that manages to pass through the entrance slit is essentially eliminated, thus only components of scattered light are transmitted through the double monochromator.

During routine investigation of the double monochromator light path, some problems were observed when examining the internal optics. The light-path and slit response did
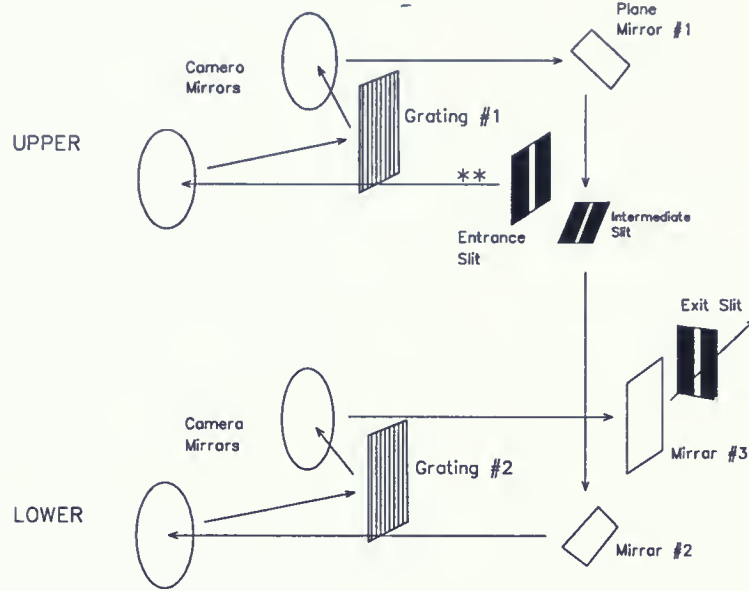
Figure 3.1: Double Monochromator Layout.

not seem to correlate exactly as outlined in the instrumentation manual [12], although it was very difficult to gain access to the optics to judge this. We were advised by Dr. R. Hackl, well known for his work on Raman Scattering in High T_c superconductors using a similar instrument, that the alignment procedure is extremely onerous and to only invoke it if deemed absolutely necessary. As will be shown in this thesis, the alignment procedure, which has not yet been undertaken, will be necessary to obtain high resolution spectra. Hackl also noted that the gratings were slightly grey in appearance from long term use and may need to be replaced later [13].

3.1.1   Slit Operation

Slit widths, particularly that of the exit slit, are of significant importance in grating spectroscopy. They provide the "selectional" capability of the spectrometer to separate frequency components moving through the system. Hence, reporting their values to a good deal of precision is required. During this work, the simple act of recording slit sizes posed a problem. The manual outlined several models with different calibration schemes for the graduations marked on the slit assembly. However, the slit assemblies (see Figure

3.2) on the spectrometer gave no model numbers. Thus, initially we could not identify the slit assemblies being used on the monochromator and consequently, could not convert the reading of the number graduations indicated on the slit scales into an actual slit dimension. During the course of the work slit dimensions were recorded via the number of scale graduations. However, ultimately the time came when actual widths were required. The following three points outline how we concluded which model corresponded to that employed on our spectrometer.

Visual verification: While the manual initially outlines several available slit models, all photographs, diagrams and descriptions of slit assemblies (entrance, intermediate, exit) found in further sections of the user manual matched those on the actual system.

Operational verification: The dial and scale readings on the slit assembly while in normal operation followed the operational description outlined in the appropriate manual section for the model described above. The manual states that one full revolution on the slit dial control knob (marked in graduations of 0-100) represents 200 μm (0.2 mm) up to 500 μ (0.5 mm). After this point one full revolution represents 500 μ. This implies that after 0.5 mm, each revolution adds 0.5 mm. Referring to Figure 3.2, we see that this gives the entrance and intermediate slits a range of 0 - 4.0 mm and the exit slit a range of 0 - 3 mm (although 4 appears on the scale!?).

Scale verification: A test was improvised to try to verify that the scheme observed above was indeed correct. A small piece of 1.0 mm diameter solder wire was placed very carefully in the lower region (below centre) of the entrance slit jaws. The jaws were then carefully closed onto the soft wire using the dial control. When fully closed to the width of the wire the reading was slightly above 1.0 on the main scale, thereby verifying a known width to the postulated scheme.

It is generally accepted that the resolution of power spectra are directly proportional
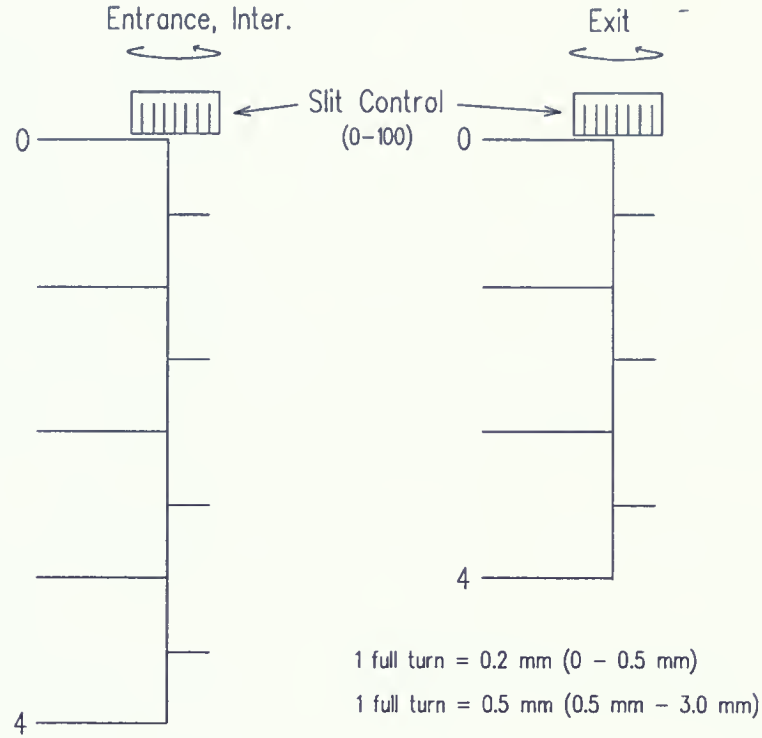
Figure 3.2: Slit control and Scale.

to the exit slit size [3], [14]. As seen later in chapter 7, our best results were found with the exit slit set at 2.5 mm, which is significantly higher than the 30 μm, 50 μm, 100 μm and 200 μm (0.01 mm, 0.03 mm, 0.05 mm, 0.10 mm and 0.20 mm) used in [3]. This is discussed further in chapter 7. The theoretical bandwidth of the spectrometer used in this work seemed on par with typical instruments [15]. To calculate the bandwidth and ultimately, the minimum useful slitwidth, one first finds the resolution limit of the grating as;

$$\frac{\nu}{\Delta\nu} = N \cdot g^{-1} \cdot d = 1 \cdot \frac{1180 \; lines}{mm} \cdot 102mm = 120 \; 360, \tag{3.1}$$

where N, g and d are the diffraction order, grating period and grating width respectively. Next, we refer to the spectrometer manual, to find a typical working angle of the grating near the wavelength of light being used [12], in our case ≈ 5145 $\mathring{A}$. This is given as;

$$\beta = 18^{o} \; (at \; 5215 \; \mathring{A}). \tag{3.2}$$

Using β, g and the focal length, f (1.0 m), of the spectrometer we may find the lateral dispersion;

$$\frac{d\lambda}{dx} = \frac{g}{f} \cdot cos\beta = 0.80598 \ nm/mm. \tag{3.3}$$

And finally from the lateral dispersion we can calculate the *bandwidth* by multiplying it with the slit width used. Thus, for the typical 2.5 mm used in this work this implies a *bandwidth* of $\approx$ 2.01495 nm or 20.15 Å. The minimal useful slit width is reached when the bandwidth equals the resolution limit of the grating. Hence is found by;

$$\Delta x = \frac{\lambda}{N \cdot g^{-1} \cdot d} \cdot \frac{f}{g \cdot cos\beta} = 5.30370 \ \mu m \tag{3.4}$$

To achieve optimum resolution of the instrument one should operate as close as possible to the minimum useful slit width. Clearly that is not the case for the work here, where the slit dimensions used were orders of magnitude larger. Further discussion on slit and resolution problems is given in chapter 7.

3.2 Laser and Power Source

Providing a monochromatic point source is a *Coherent Innova 90* Kr-Ar mixed gas Laser. The laser is powered by its own dedicated 240 V mains feed and cooled via a water-jacket surrounding the gas chamber. This is fed by a 5/8" water hose which requires a minimum flow rate of 8.3 L/min at 1.8 kg/cm^2 and a maximum inlet temperature of 35°C. [6]

The laser is capable of emitting several laser lines at different wavelengths and varying power by selection from a control dial at the rear of the laser. Previous work done by [6] found these lines include:

WAVELENGTH (Å)	COLOUR	POWER (W)
4579	Blue	0.17
4658	Blue	0.07
4727	Blue	0.16
4765	Blue	0.48
4825	Blue	0.008
4880	Blue	1.4
4965	Blue-Green	0.45
5017	Blue-Green	0.2
5145	Green	1.5
5682	Yellow	0.05
6471	Red	0.25

Table 3.1: Possible Laser lines and associated Power.

3.3 Detector and Photomultiplier

An *Electron Tubes P10232* photodectector is used to detect the Raman scattered radiation. This model consists of a photomultiplier tube with a 22mm active photo-cathode area. DC current is converted to a 100 - 1300 V potential acting across a 10 dynode chain which amplifies the very "small" signals that reach the detector window. Typically, the detector was used in photon counting mode as recommended by the manufacturer for measuring the most sensitive or short lived signals. [16]

Understanding the operation of the detector is best done by considering the particle nature of light. Each photon which strikes the photocathode has a probability of releasing a photo-electron depending on its frequency (or wavelength). This photo-electron is then accelerated across the first dynode by the high voltage, where it strikes the second dynode. Upon impact it releases a number of secondary electrons which are then accelerated to the third dynode, etc. Ultimately, upon exiting the dynode chain the previous incident photon is converted to a mV signal which is then amplified and sent to the computer for analysis [16].

In the green (5145 Å) range the Bi-alkali photocathode operates with a quantum efficiency of approximately 18%. At 4000 Å (Blue) it has a quantum efficiency of 25%

[16] and since scattering intensity is proportional to ω^4, these factors may be taken into account to increase signal size [5]. The Holographic Notch Filter (see section 3.4) required to operate at 4880 Å is a significant cost and since this work focused on overall optimisation of the system, it was decided to continue using the Green 5145 Å line. Following optimisation work, if one were to use the Blue 4880 Å line, sensitivity should improve.

The temperature of the detector also directly affects its responsivity. During this work it became necessary to introduce a Peltier cooling arrangement to improve sensitivity and thermal stability of the detector. A considerable amount of work was done to find the optimum setting for the Peltier cooling attachment, the results are discussed in chapter 5.

3.4   Optical Components

Throughout this work no changes were made to the laser model, monochromator, detector or computer, however, the collection optics were redesigned to allow for extra space to manouver components, the addition of optical components and the inclusion of a cryostat for temperature dependent measurements.

Calibration and optimisation work was carried out on both the original and redesigned arrangements. In each case all experimental procedures and methods remained the same. A description of the individual arrangements is given in the following two sub-sections.

3.4.1   Original ('Old') Collection Optics

The first arrangement consisted of a "chamber" which was directly attached to the monochromator housing with sealed seams. The optical components were attached to its walls. As seen in Figure 3.3, the propagating laser beam was manipulated to allow the incident light to strike the sample. This set-up employed translationally fixed mirrors
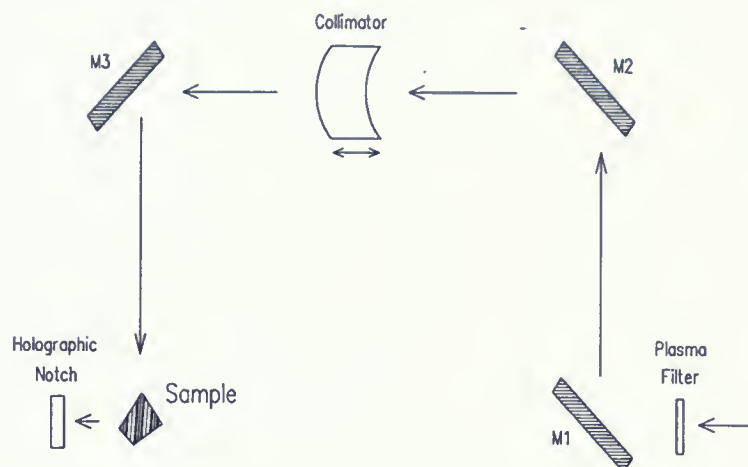
Figure 3.3: Schematic showing **initial optics** arrangement. (Side View).

(could only rotate), the collimator lens had limited travel and no additional optical components or cryostat could be added. It was decided to move to a breadboard arrangement after some calibration and optimisation work had been completed.

3.4.2   Modified ('New') Collection Optics

Providing a base for the new collection optics arrangement is a 3/4" solid Al plate. 36" x 38" with 1/4"-20 holes tapped on a 1" square grid pattern. All post stands have double slotted baseplates which allow for secure fixing of heavy components **anywhere** on the breadboard [17]. The breadboard and post stands were designed and machined in house in order to be cost effective. The coverage of the board also allows generous space for additional optics and a cryostat. As seen in Figure 3.4, this arrangement manipulates the laser path so that the incident light strikes the sample at an angle of approximately 25°-30° from the plane of the sample face and the scattered radiation is collected near 90°. This is similar to the arrangements proposed by [18] and [19]. To protect the optics from any stray/ambient light, an in-situ cover was made from a large cardboard box. The interior of the box was painted with black, flat finish paint and had dark absorbant felt placed between box edges and any apparatus contact seams.
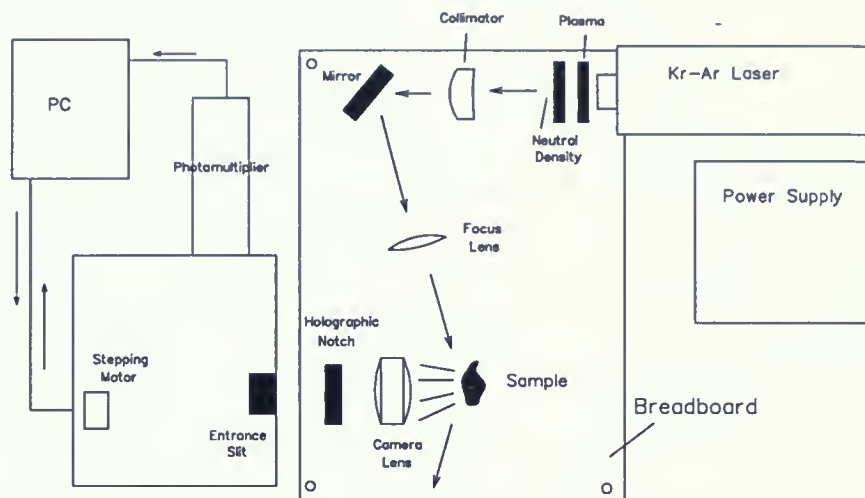
Figure 3.4: System schematic showing **final optics** arrangement (Top View). Neutral Density Filter and Focus Lens, optional.

3.4.3 Cold-Finger Cryostat and Sample Stage

Implementation of a cryostat allowed temperature dependent Raman measurements to be carried out on samples. Raman spectra could be collected at temperatures as low as 4K and beyond 293K. The cryostat consists of a copper *cold-finger* fed with a monitored flow of liquid Helium or Nitrogen which cools the sample via thermal contact. The sample stage and chamber is shown in Figure 3.5. An integrated heating coil allows measurement at any "intermediate" temperature by providing a small amount of heat energy, balanced with appropriate monitoring of the cryogen flow. Temperatures above 293K are also accessible by omitting the use of any cryogen and simply using the heating element. However, the heater and associated thermocouple cannot exceed 350 K [20].

Incident laser radiation is directed through a small 1.5" quartz window, allowing scattered radiation to be collected via a 2.0" quartz window at 90°. A vacuum flange opposite the incident window provides the means to evacuate the sample chamber. Typical values for the operating vacuum were on the order of 10^{-6} - 10^{-7} torr.

During preliminary work it was found that using liquid Nitrogen proved problematic. The higher density liquid (relative to Helium) requires a dewar that is capable of being pressurized beyond 10-12 psi to allow for sufficient flow through the transfer tube to cool
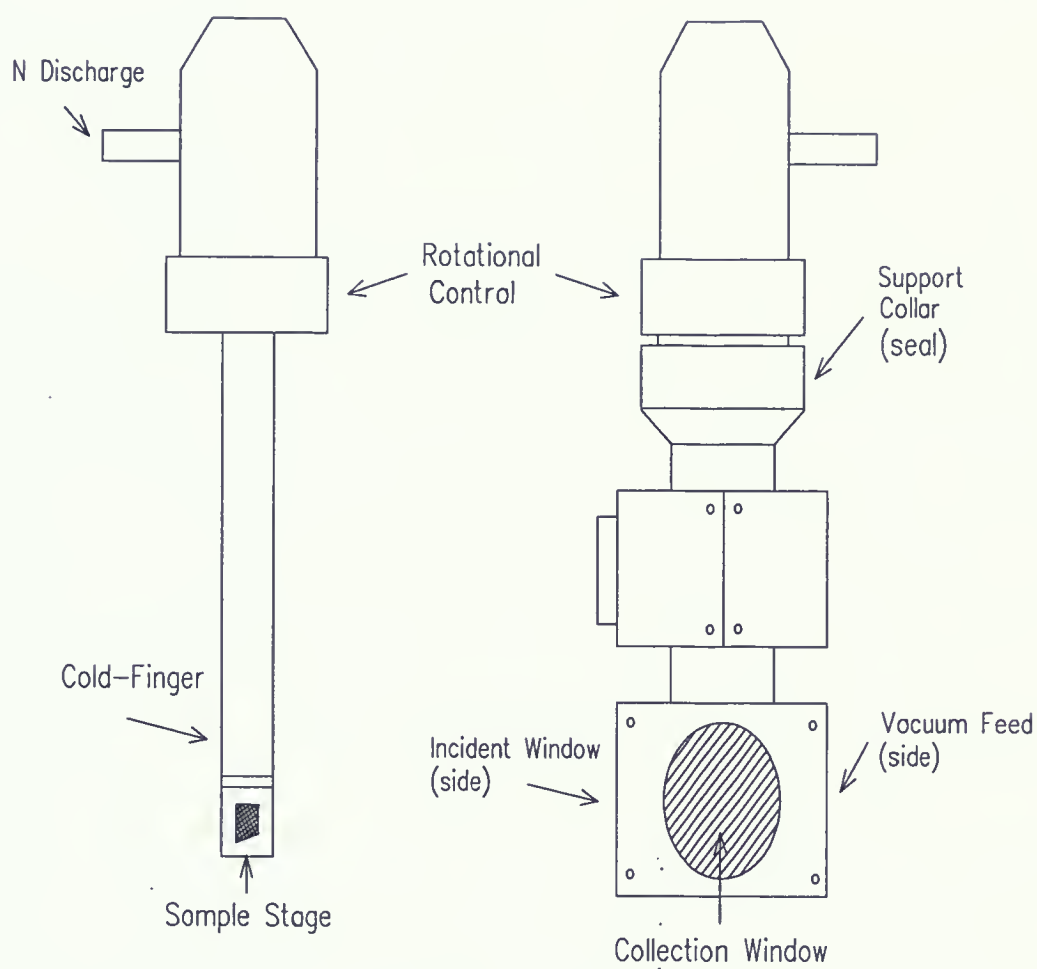
Figure 3.5: Cold-Finger cryostat arrangement.

the cryostat down to 77K. It is more favourable to use liquid Helium, which is much easier to transer and control the flow. Liquid Nitrogen temperatures or any other intermediates can be obtained by utilizing the integrated heater and monitoring the flow of Helium (via pressurization of the He storage dewar with He gas and the use of a flow meter). During low temperature runs care needed to be taken to prevent damage caused by frost forming on and around the cryostat. A *Variac* power supply connected to a heating jacket on the cryostat provided adequate protection.

3.4.4   Filtering

Filtering is an extremely important part of any optics system and is especially important in a Raman set-up. The typical ratio of Raman (inelastic) scattered radiation to incident radiation is on the order of 10^{-6} - 10^{-7} [9], [4]. Thus, even though a double monochromator arrangement provides a good deal of "wavelength selection", careful filtering of unwanted components is required to maximise the amount of scattered light that reaches the detector. Specifically, for Raman scattering the two significant components that must be eliminated are: *Plasma Emission Lines* and *Elastically Scattered* light.

Reflected light is easily eliminated by directing the reflected beam to a laser stop arrangement.

Plasma emission lines are a direct result of stimulation of electrons inside the excitation chamber. The large potential (V) acting across the Kr-Ar gas stimulates electrons to higher transitional states at varying wavelengths (frequencies). Consequently, an Intensity vs. Wavelength spectrum would show peaks of varying intensities across the wavelength range. Since we are solely interested in the Intensity vs. Wavelength spectrum of the sample being measured, these plasma lines must be eliminated or they could potentially distort the Raman spectrum of the sample. Common procedure dictates the use of a high quality bandpass filter to achieve this. An *Oriel 52660 #3* bandpass filter was placed directly in front of the Green 5145 $\mathring{A}$ laser source. The filter with a bandwidth

of 10 $\mathring{A}$ allows only a narrow band of light to pass through, centred at 5147 $\mathring{A}$ [21].

The scattered radiation passes through a Holographic Notch Filter before entering the monochromator. The role of the notch filter is to eliminate elastically scattered (Green) light. A *Kaiser Optical Systems, Super Holo-Notch* filter at 5145 $\mathring{A}$ is employed. A half-width of 100 $\mathring{A}$ implies that it eliminates light in the approximate range of 4195 $\mathring{A}$ to 5195 $\mathring{A}$ [22]. This is clearly an appropriate Bandpass and Notch-Filter pair, since the acceptance range of 5142 $\mathring{A}$ - 5152 $\mathring{A}$ lies well within the notch cut-out range of 4195 $\mathring{A}$ to 5195 $\mathring{A}$.

A *Neutral Density* filter was used to reduce the overall intensity of radiation when scanning near or across the laser line. These filters act in a similar manner to partial mirrors. Some light is allowed through the filter and the rest is reflected back. The number quoted on each filter states how much (%) of incident light is transmitted through the filter. For instance, a 0.7 Neutral Density filter blocks 99.3% of the incident radiation. I.e. 0.7% is transmitted.

3.4.5   Lenses and Mirrors

Mirrors used in both the original and modified optical arrangements were salvaged from the donated system since they were of good quality. Inspection of the mirrors showed that they were coated for optimum reflection, ideal for use with laser systems. Two lenses were used in the modified optical setup: One collimator lens and one *Miyoto* f/8, 55 mm camera lens which served to capture and focus the scattered light onto the entrance slit plane. Refer to Figure 3.4.

A double-convex lens was also used to focus light from mirror #1 into the cryostat and onto the sample surface. However, the double monochromator seemed particularly sensitive to any alignment changes and no apparent gains were realised from its use. A cylindrical lens would be another choice for future improvements, since the incident light strikes the sample by glancing across it and causes an elongated illumination spot.

Concentrating the illumination spot allows one to select nice areas on a sample surface containing imperfections, however, one must take care to avoid surface heating effects which could be detrimental to the measured Raman spectra. This is usually not a problem, especially for solid samples, as the threshold for adverse heating effects (melting) is approximately 400 mW (0.8 μm spot size, 5145 Å linearly polarised) [23]. In this work, power near the sample surface was usually maintained at approximately 75 mW and never exceeded 100 mW. Low temperature measurements in this work were carried out using laser powers in the range of 66.2 mW - 87.7 mW, with an elongated (oval) illumination spot that measured approximately 2.5 mm by 1.0 mm. An elongated or line focus can be used on samples with near perfect surfaces to reduce the power density. This is especially useful for low temperature measurements.

3.5 Computer Control and Software

A C^{++} encoded program designed by [2] is used to collect and display the Raman power spectra. The windows interface allows the user to select the range and collection settings of the detector. The five important settings are: *Check Motor Interval, Motor Stop Delay, Delay While Gathering, Photomultiplier Wait Time,* and *Readings Per Sample.*

Check Motor Interval controls the "frequency of checks" at which the computer verifies the motor has stopped. The Motor Stop Delay serves to avoid any problems from motor drift. After the program detects the motor has moved to the next wavelength position and stopped, the computer waits for the specified time to ensure it has completely stopped. The program then waits again for the user specified, Delay While Gathering, which then allows the photodetector to adjust to the new wavelength position. Following this, the software then begins collecting intensity data for the duration of the Photomultiplier wait time. If more than one (1) Reading Per sample is specified, the sampling process is repeated until complete. Using multiple Readings per sample at a particular wavelength

point results in a much higher overall count. This is due to the software which adds all readings at a particular wavelength position and displays the sum result. This implies that the reading at that point has a much higher signal to background ratio, hence yielding a "smoother" plot. The program then moves on to the next specified wavelength and the entire process is repeated [2]. These parameters and the collection process are explained further in chapter 5.

For each wavelength selected within the specified range, an intensity measurement in mV is displayed via the detector and software. All points collected make up the Raman spectrum which gives a plot of scattered intensity (arb. units) vs. wavelength (Å). The wavelength data is readily converted to frequency (cm^{-1}) by a simple conversion calculation.

Chapter 4

# Experimental Methods and Procedures

4.1 Plasma Line Scans

As introduced in Sect. 3.4.4, Plasma or emission lines are a consequence of electronic transitions made by stimulated ions in the laser's excitation chamber. Since these lines are caused by well known quantum mechanical processes they are essentially the same for any laser of the same type. Minor variations may exist for different temperatures [24]. However, this can be controlled using a cooling arrangement as outlined in Sect. 3.2. Since the emission lines provide a universal standard, they were employed to find the relationship between Wavelength displayed or "Monochromator Wavelength" and the True Wavelength.

It was found that the best plasma line scans were taken with the laser power set at approximately 8.5 mW, with no neutral density filters in place. The neutral filters introduced noise that made viewing of the plasma lines difficult or impossible. This effect is demonstrated in Figure 4.1 and Figure 4.2 Once a scan had been taken, it could then be calibrated approximately using a linear equation found by [2] or [6]. These are summarised in Table 4.1 below. The reader is encouraged to read references, [2] and [6] for more information on the calibration method used to calculate each calibration equation. This graph could then be compared to literature values by super-imposing the literature peaks (emission lines) onto the experimental peaks found for the Plasma line scan. By using the cursor position in the graphing software, pairs of points could be found that correlate to (Monochromator Å, True Å) = (X,Y). This then provided a basis
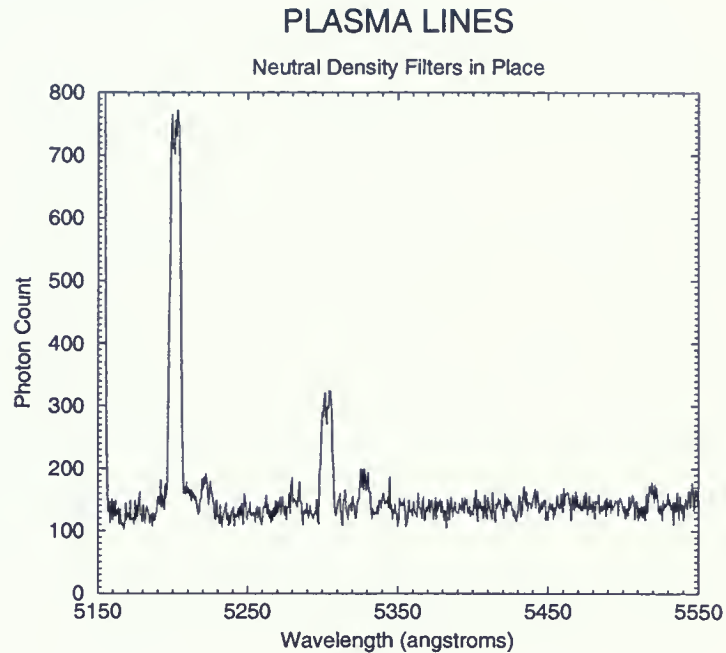
Figure 4.1: Effect of Neutral Density Filters on Plasma Scans. 1.00s sample time per data point.
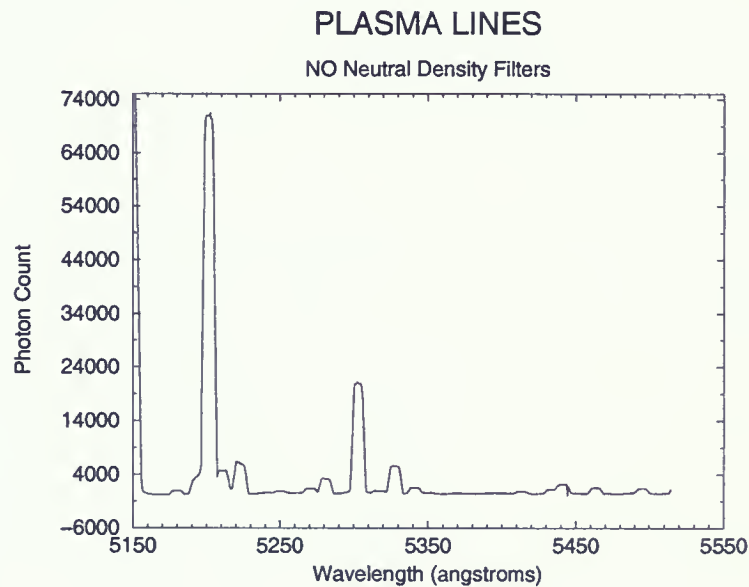
Figure 4.2: Plasma Line Scan with **no** Neutral Density Filters. 1.00s sample time per data point.

Equation	Calibration Method
y=1.225509x - 1245.4280000	Maximising laser lines with Si diode and Oscilloscope
y=1.226154x - 1246.7550838	Simple Diffraction Equation measuring Dist. from m_0 to m_1

**Table 4.1:** Previous Calibration Equations.

for a linear regression fit.

It should be stated that the accuracy of this method does depend somewhat on the individuals capacity to determine the centre of the plasma peaks and match them with the literature values. However, if one draws a line through the approximate peak centre and uses the displayed x-value, it provides a good basis for determination. Some attention should also be given to the accuracy of the displayed cursor position. The software used in this thesis, *XMGR*, typically displayed the cursor position within 0.2 - 0.3 % of the true data point value. A select number of scans were calibrated using two - forty three identified plasma lines. This was the result of iterative work using the above method. Originally, only 2 lines were used, but as the calibration equation found became more and more accurate it allowed other peaks to be identified. Appendix A tabulates the literature positions of the plasma lines and shows them super-imposed on an experimental plasma line spectrum. Shown in Figure 4.3 is an example of the linear relationship derived from plotting literature plasma peak positions versus monochromator display. From the calibrated scans, a number of successively better, linear equations were derived. Table 4.2 summarizes the calibration equations found in this work.

Using the calibration equation derived from the 43-point fit, one may calculate the true position of Optical Modes or Shifts from the incident laser line. For example, [14] locates the 1st TO phonon mode for Silicon at 520.2 cm^{-1} from the incident laser line. Other values for shift are 519 cm^{-1} and 520 cm^{-1} reported by [25] and [26]. To verify this using our calibration equation, we first locate the peak/line centre. Looking ahead to chapter 7, Figure 7.5 presents the 1st TO phonon mode for Silicon at $\approx 5324.51\text{\AA}$ in terms of

TRUE vs. MONOCHROMATOR

wavelength calibration

$y = 1.219872x - 1209.31$
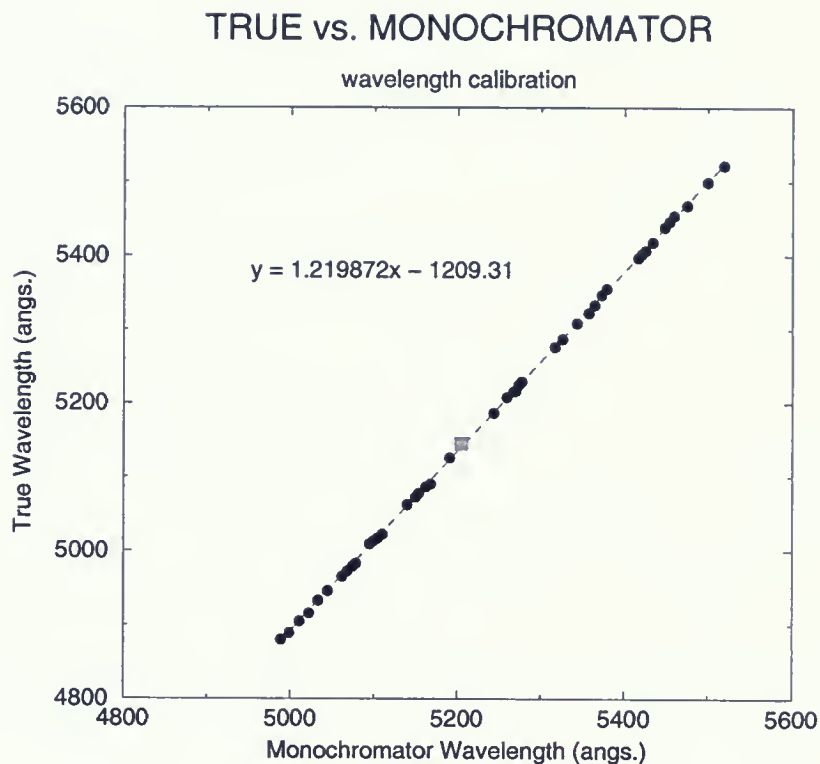
Figure 4.3: Linear Relationship of True Å vs. Monochromator Å. 43-point fit showing laser line as grey square.

No. Points in Fit	Calibration Equation	Optics Arrangement
2	$y = 1.345760x - 1902.38$	old (original)
3	$y = 1.074820x - 460.952$	old
4	$y = 1.074260x - 457.997$	old
6	$y = 1.103640x - 613.076$	old
10	$y = 1.170080x - 956.551$	old
13	$y = 1.171190x - 962.067$	old
18	$y = 1.220450x - 1211.96$	old
23	$y = 1.221102x - 1215.87$	new (modified)
43	$y = 1.219873x - 1209.32$	new

Table 4.2: Calibrations Found in This Work.

monochromator wavelength. Shifted from the true 5145Å laser line. Thus, referring to Table 4.2, this shift is converted to true wavelength using;

$$y = 1.219873 \cdot (5324.51 \text{ Å}) - 1209.32 \text{ Å} = 5285.91 \text{ Å} = 18918.23 \text{ } cm^{-1}. \tag{4.1}$$

The 5145 Å laser line is located at;

$$5145 \text{ Å} = 19436.35 \text{ } cm^{-1}. \tag{4.2}$$

Thus, the shift from the Laser line for the 1st TO phonon mode is given as;

$$19436.35 \text{ } cm^{-1} - 18918.23 \text{ } cm^{-1} = 518.11 \text{ } cm^{-1}, \tag{4.3}$$

which is in reasonable agreement with the literature values given above. Note that in Table 8.1 the same phonon is found at 521 cm^{-1} at 293 K. As will be discussed in chapter 7, this variation in identifying the peak centre is likely the result of poor resolution.

Other fits, such as exponential or logarithmic can be used. However, it was found that over the range of each scan done the exponential or log fit was essentially linear throughout the range and there was no apparent advantage in changing to a non-linear regression. Consequently, we are left with a simple linear relationship between the True wavelength (y) and that displayed by the Monochromator (x).

4.2 Sample Mount and Stage (Pre-Cryostat)

Prior to installing the cryostat, samples were mounted on an X-Y-Z stage arrangement with a heavy base for vibration isolation and stability. An arm projecting from the apparatus allows for the attachment of a rotating sample stage. The rotation may be used to vary the angle of incidence of the illuminating light. See Figure 4.4. The sample
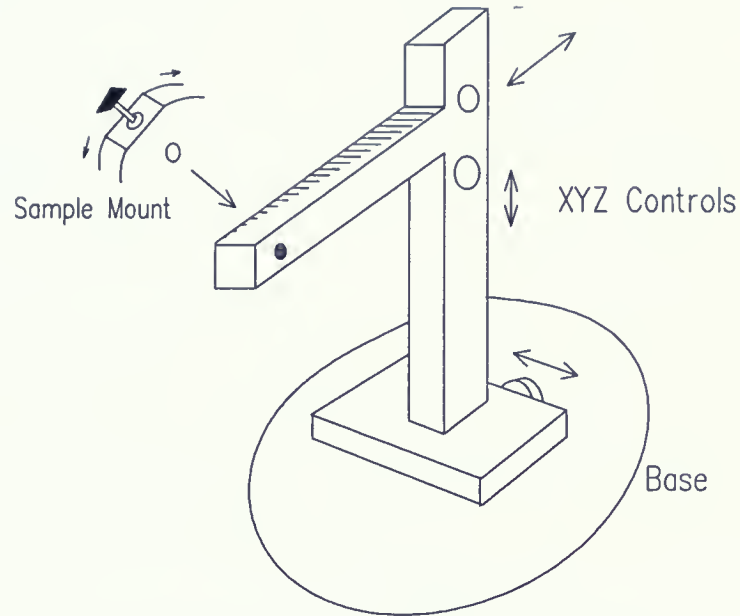
Figure 4.4: X-Y-Z and sample stage.

may be attached to the sample stage surface via vacuum grease. However, the best results were obtained by using a mount that spatially separated the sample from the sample stage surface. This was achieved by mounting a small brass pin via epoxy, perpendicular to the sample stage surface. The sample could then be glued to the tip of the pin. Dark absorbant foam on the stage surface provided protection from stray reflections contributing to the scattered image and entering the monochromator with the scattered light. The grease mounting arrangement and sample pin mount are shown in Figure 4.5. Of course, when using the cryostat sample stage, the best method is the one that provides the most thermal contact with the *cold-finger*. Hence, the grease mount arrangement was used with the cryostat.

4.3 Silicon

Following initial calibration work, attempts to measure the Raman spectrum of crystalline Silicon were undertaken. Silicon possesses a bi-atomic basis per unit cell, with a Diamond or Face-Centred structure. It belongs to the O_h^7 space group, thereby having
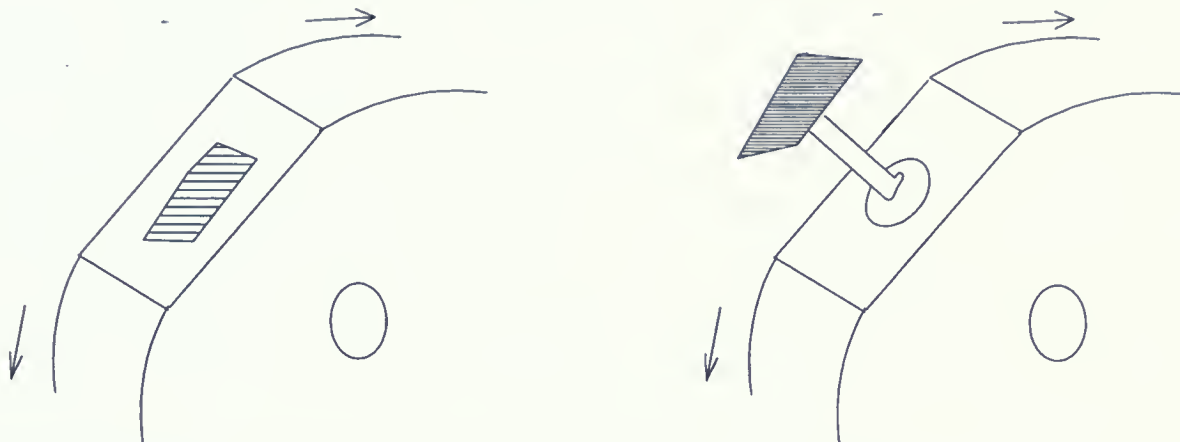
Figure 4.5: Two Different Sample Mounts. Grease mount on left, pin mount on right.

only one 1st order Raman active phonon mode located at the zone centre (k=0) [25]. It's simple structure has been extensively studied in the literature, thus provides a definitive comparison for the work completed here. The goal of this section was to see if a Raman spectrum of the 1st TO phonon mode could be viewed. This would provide a starting point from which optimisation work could begin.

Initially, the Silicon wafer sample was mounted using the vacuum grease arrangement as outlined above (Figure 4.5). It was estimated that the laser made an incident angle with the Si of approximately 40°. The resulting spectrum showed no visible evidence of any optical modes. Upon further inspection it was found that laser light was not only striking the sample, but also the sample stage surface. This created a secondary contribution to the collected light. Not only was scattered light entering the monochromator from the Silicon wafer, it was also coming from reflected/scattered light via the sample stage surface.

When the incident angle was changed to approximately 25° [27] and the "Pin Mount" described above was used, the spectrum shown in Figure 4.6 was observed under the same collection settings. Although of poor quality, the Silicon TO phonon mode is visible. Having made these changes it was decided that the next course of action would
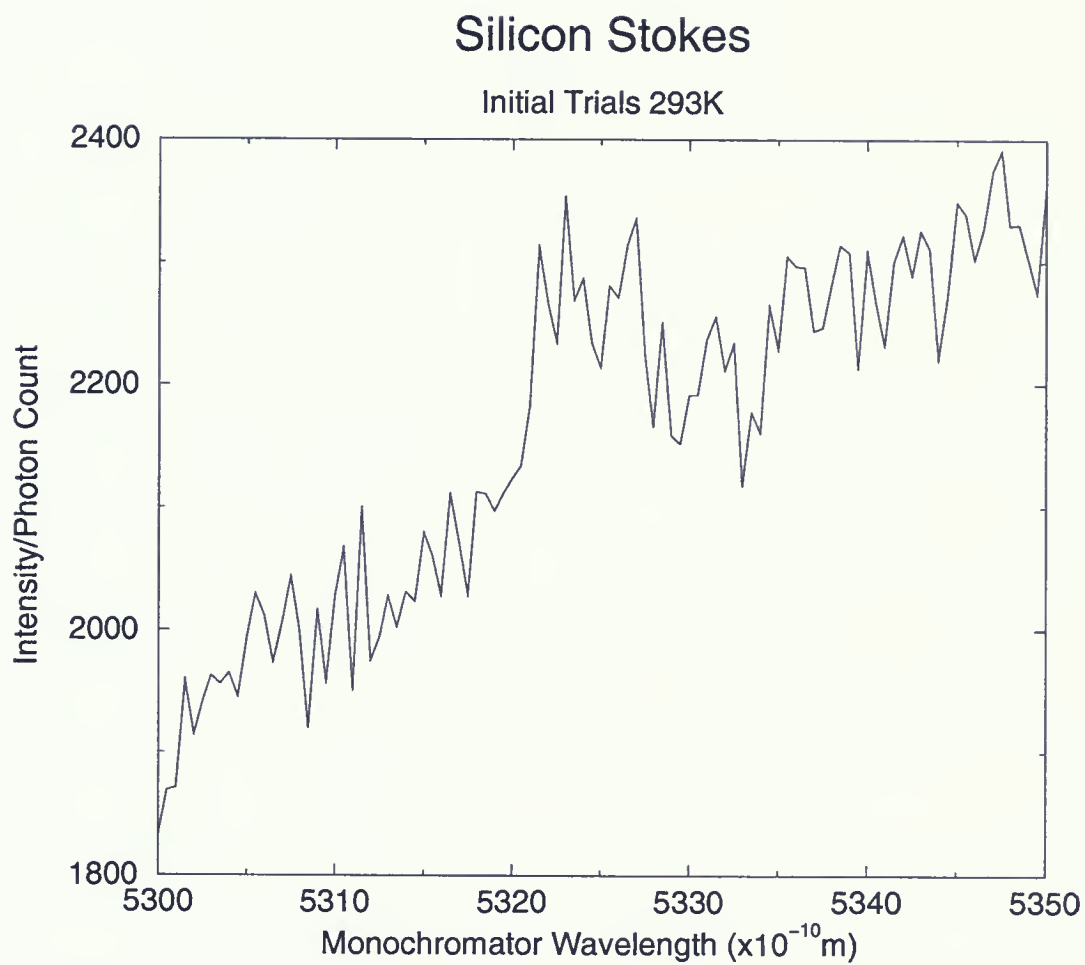
Figure 4.6: First Silicon scan. 10.0s sampling time per data point.

be to undertake the optimisation of the software settings designed by [2], which had never been carried out.

Chapter 5

Optimisation of Collection Software Settings

To obtain good quality spectra, one must be sure to collect under the best possible conditions. An important fact to consider is the "wait-time" under which sampling occurs. This system uses a number of collection parameters which are used to control different aspects of the collection process. Ultimately, the goal of this chapter is to show the overall nature of the collection parameters and how they affect the quality of spectra obtained. For this reason, since we need to know how they affect spectra in an objective manner, silicon was abandoned for the time being and all measurements were taken using the 5308.7 $\mathring{A}$ Plasma line.

5.1 Collection Parameters Explained

The C^{++} program designed by [2] allows for manual adjustment of five (5) separate collection parameters, provided to the user in Preference windows. They are;

- CMI, Check Motor Interval (Check Motor Stop)

- MSD, Motor Stop Delay

- DWG, Delay While Gathering

- PWT, Photomultiplier wait time

- R/S, Readings per Sample

CMI and MSD make up the two "pre-collection parameters". CMI sets the interval at which the program checks to see if the motor has stopped, a setting too high greatly

increases the scan time required, while a very low setting limits the ability of the computer to physically check the counter at a given wavelength. MSD controls the time to wait after detecting that the motor has stopped. This allows for compensation of any drift in the motor after the power is cut.

The actual sampling period takes place after the MSD period and is controlled by three other "collection parameters" namely, DWG, PWT and R/S. The DWG follows the MSD and allows for manipulation of the time for the detector to adjust to a particular wavelength. Once adjusted, the computer then waits for the PWT period, where intensity data is collected via the photomultiplier for the wavelength of interest. It is also advantageous to have more than one Reading per Sample at a particular point, hence the R/S setting can be set to collect only once or up to 255 times at a particular wavelength. On multiple Readings per Sample, the software waits for the specified PWT and then repeats the PWT reading up to the user defined R/S. The result is a cumulative, larger overall reading resulting in a better ratio of signal to background.

Of course, increasing any and all collection parameters yields a much higher net wait time per wavelength sampled. Thus, depending on the size of the scanning region it may be useful to minimize or find the most optimum (smallest time, high quality) settings for the collection parameters. Thereby, allowing one to scan in the most efficient manner. It was decided after some initial work to focus on optimising the three dominant collection parameters; DWG, PWT and R/S. CMI and MSD were left to their default values of 0.1s and 1 s respectively. A CMI period of 0.1s was seen as a good operational setting since it provided a relatively high "frequency of checks", to verify the motor was stopped and was not extremely low (i.e. 0.01s). The MSD was left at 1.0 s since, any motor drift could always be compensated by a slightly higher DWG.

Given in Table 5.1 are the two groups of tests designed to find the optimum settings of the three dominant collection parameters and discern their overall effect on the spectrum. Tests 1 - 4 were designed to understand the relationship between PWT and R/S

| TEST NO.	MSD (s)	DWG (s)	PWT (s)	R/S
1	1.00	2.00	2.55 MAX	1 MIN
2	1.00	2.00	0.01 MIN	255 MAX
3	1.00	2.00	0.01 MIN	1 MIN
4	1.00	2.00	2.55 MAX	255 MAX
5	1.00	0.01 MIN	2.55 MAX	25
6	1.00	10.0 MAX	0.01 MIN	25
7	1.00	0.01 MIN	0.01 MIN	25
8	1.00	10.0 MAX	2.55 MAX	25

Table 5.1: Test Summary: Optimising Collection Parameters.

on the spectrum. It was estimated that PWT would increase the signal size, since the photodetector remains at a particular wavelength for a longer time. Hence, more photons are counted. Multiple R/S give a smoother plot, since more than one (1) reading per sample is taken at each wavelength which increases the signal, while averaging out the noise. The second group of tests, 5 - 8, were undertaken to find the extent of interaction between DWG and PWT, since these two variables could potentially influence the outcome of the measurement. This is due to the fact that the DWG period immediately precedes the sampling period, PWT. Also, one needed to understand the overall effect of DWG on the spectrum.

5.2 Data and Results

The results from tests 1 - 4 and 5 -8 are shown in Figure 5.1 and Figure 5.2 respectively. The plots are organised in each figure, so that when analysing the reader may qualitatively assess the trend of increasing the working range of a given collection parameter versus another. For example, in Figure 5.1 four plots are shown and arranged such that one may assess the general effect of increasing the PWT by reading up and the overall effect
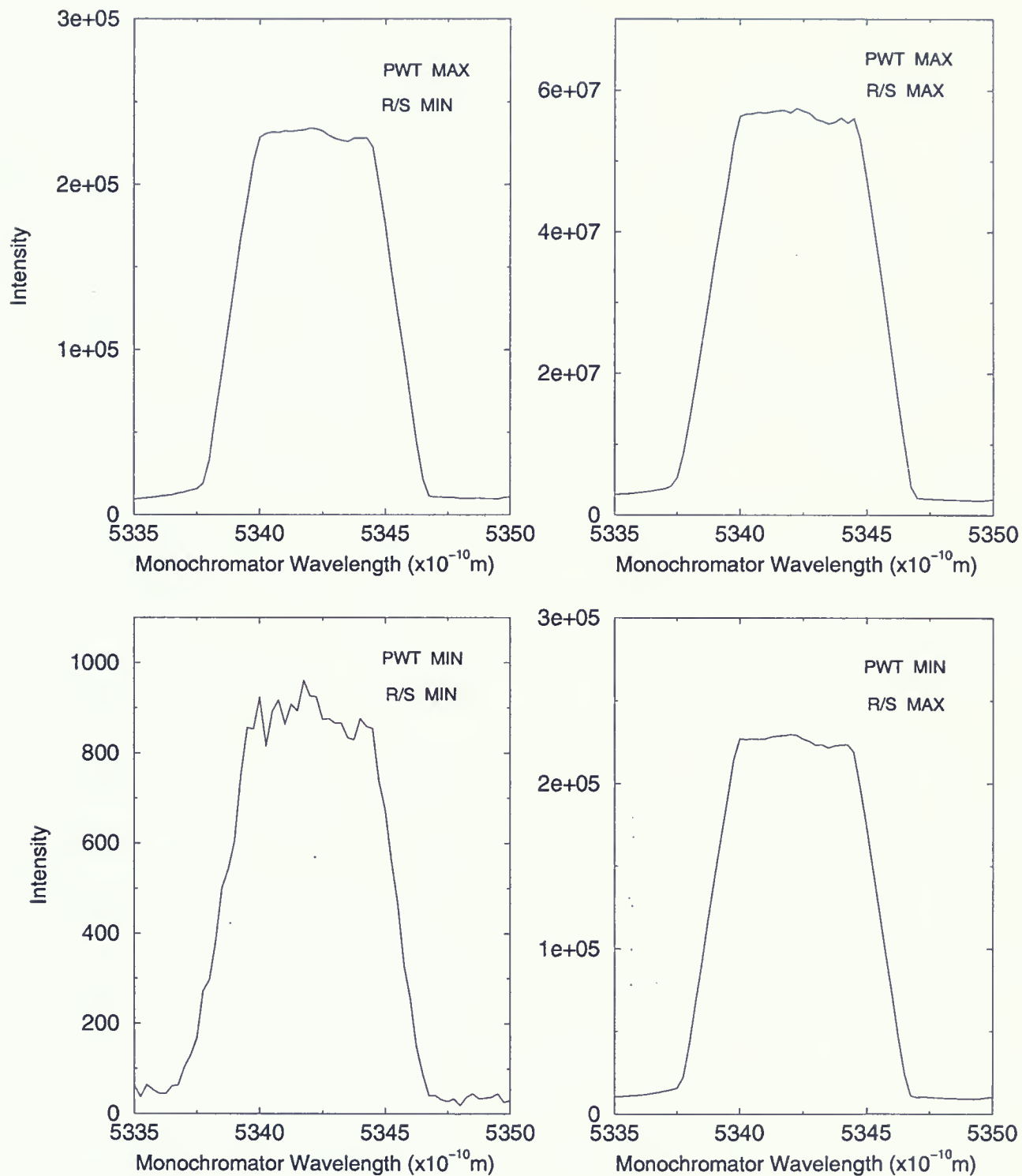
Figure 5.1: Photomultiplier Wait Time (Read ↑) vs. Reading per Sample (Read →): Using 5308.7Å Plasma Line.

of increasing the R/S by reading across.

The obvious effects of increasing the PWT to a high setting are a much higher overall photon count (intensity) and a smoother curve. This is most evident at low (MIN) R/S settings, as seen in Figure 5.1. At higher (MAX) R/S settings, significant increases in PWT have much less effect on "smoothness" and seem only to increase the overall photon count or intensity. Similarly, at low PWT settings a dramatic increase in photon count and smoothness can be obtained by a large increase in the R/S setting. However, at high PWT the effect of a comparable R/S setting is much more subtle.

Thus, we are left with two possible ways in which to optimise the spectrum to yield a given number of total counts via manipulation of PWT and R/S. Namely,

- Low PWT with relatively high R/S

- High PWT with relatively low R/S

This begs the question: Which one is the most efficient? Note that the spectrum with PWT MAX, R/S MIN has approximately the same number of total counts as the spectrum with PWT MIN, R/S MAX.

The answer to this came after some work was completed on a "scan time" estimate equation. It was necessary to find a reasonably accurate means of estimating the approximate scan time, since the software used a running average method. This implied that the time to completion was calculated by averaging the time taken to scan thus far and then using this to approximate the time left in the scan. This was problematic since the estimate changed from point to point, especially at the start of the measurement and one needed to be present for quite some time before a good approximation could be displayed. Also, if an approximation of the scan time could be made before the experiment was initiated, then this would provide much more control over scheduling and management of experimental work.

After some simple calculations based on scans already completed, it was found that

the scan time equation could be broken into three parts: collection time, movement time and a "tax" that increased with the number of Readings Per Sample (R/S), apparently a consequence of repeating collection measurements at a particular point and the increased communication time between software and the A/D card. This "tax" was found by linearly approximating the relationship between the additional time not accounted for by the first two components and the number of R/S. This yielded the final approximation for scan time in seconds (typically accurate to better than 1 %), given as;

$$T_s = N \cdot [DWG + MSD + (PWT \cdot R_s)] + \frac{(N-1) \cdot \Delta \cdot 60}{MS} + N \cdot [0.263655 \cdot R_s] \quad (5.1)$$

where MSD, DWG, PWT, R/S = R_s are defined as before. N represents the number of points in the scan, Δ represents the increment from point to point and MS stands for "monochromator speed" read in $\mathring{A}$/min. from a dial on the double monochromator. Since the increase in the number of R/S implied a significant increase in the overall scan-time, it was clear the the most efficient manner in which to scan was by using a High PWT with a relatively lower R/S setting.

Shown in Figure 5.2 are the test results comparing the effects of PWT and DWG. As outlined above, the four plots are arranged such that the effect of increasing PWT is shown by reading up and the effect of increasing DWG is seen by reading across. As in the previous group of tests, the obvious effect of increasing the PWT is a significant increase in intensity or photon count. This is evident at low and high DWG settings. There seems to be little effect of increasing DWG at high PWT. A slightly "smoother" section is seen on the Plasma Line peak, however, this may simply be due to one anomolous point. The only significant observation is that at low DWG and low PWT, a "lag" or onset feature appears in the plot. This makes sense since, the DWG feature controls the time at which the computer waits before the PWT or actual collection. Hence, at low DWG with a high PWT the time the detector needs to recover between samplings is negligible compared to
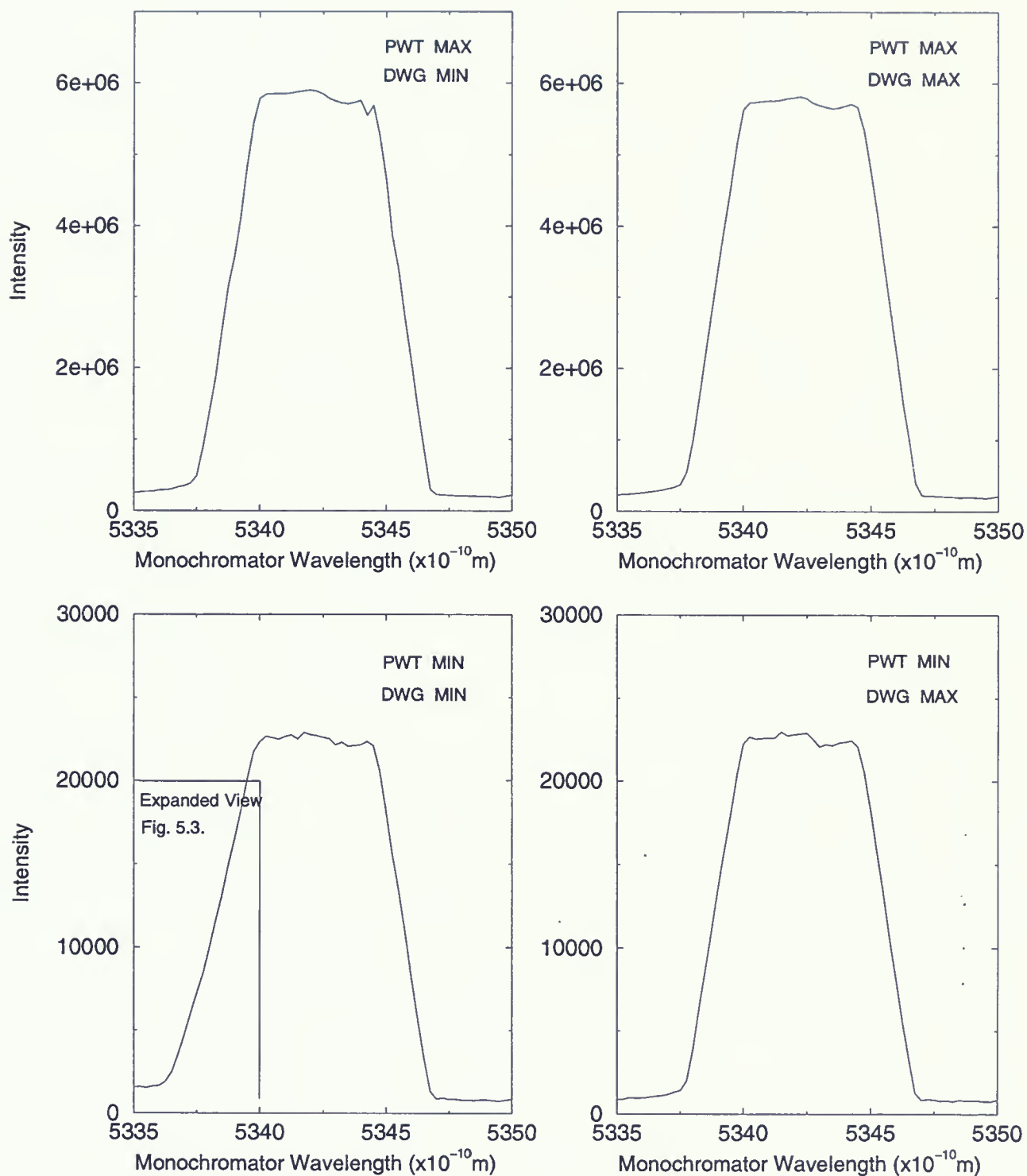
Figure 5.2: Photomultiplier Wait Time (Read ↑) vs. Delay While Gathering (Read →): Using 5308.7 Å Plasma Line.
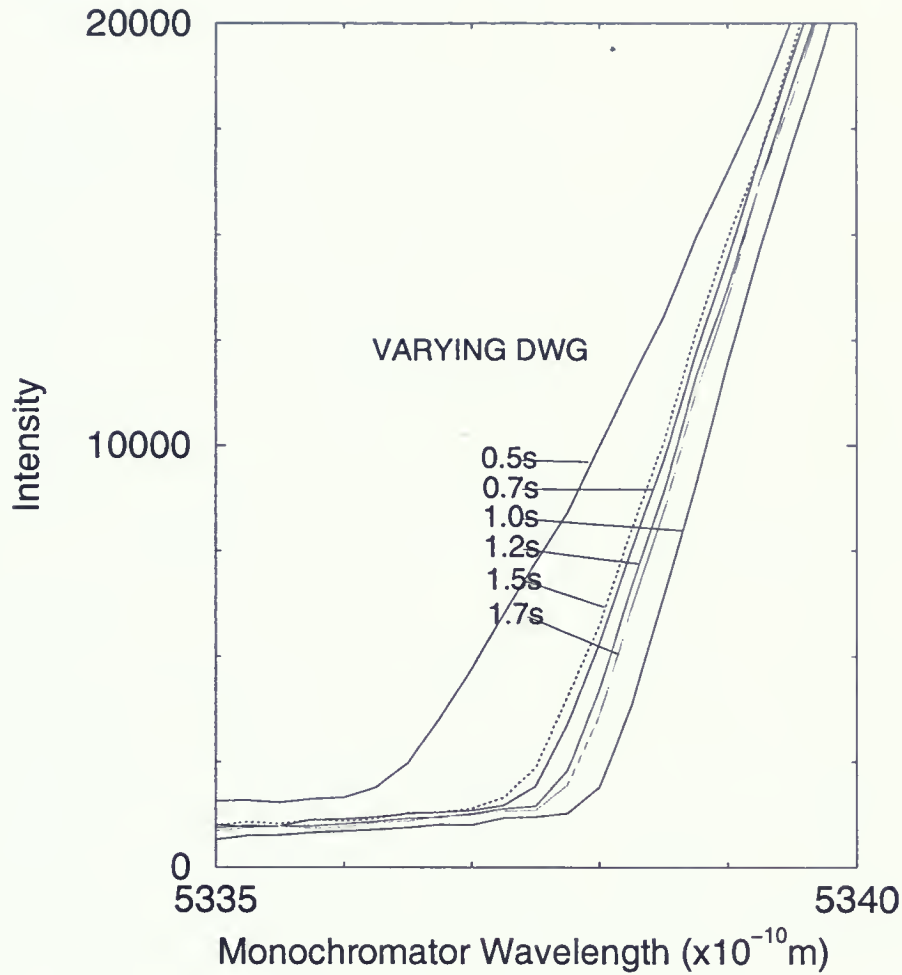
Figure 5.3: Varying Delay While Gathering.

the long counting time while sampling. However, at low DWG times and a low PWT the detector recovery time is significant compared to the collection time. A more detailed investigation shown in Figure 5.3 shows the nature of this effect. Clearly, the figure shows a slight oscillatory drifting nature. The best or narrowest peak seems to occur with a DWG setting close to 1.00s. Although due to the oscillating nature in DWG a setting anywhere between 0.7s and 1.7s would seem appropriate. This oscillatory nature is likely due to fluctuations in dark count. The important point is that a low DWG such as 0.5 s gives an artificially broadened peak due to the fact that the detector is unable to recover properly between readings.
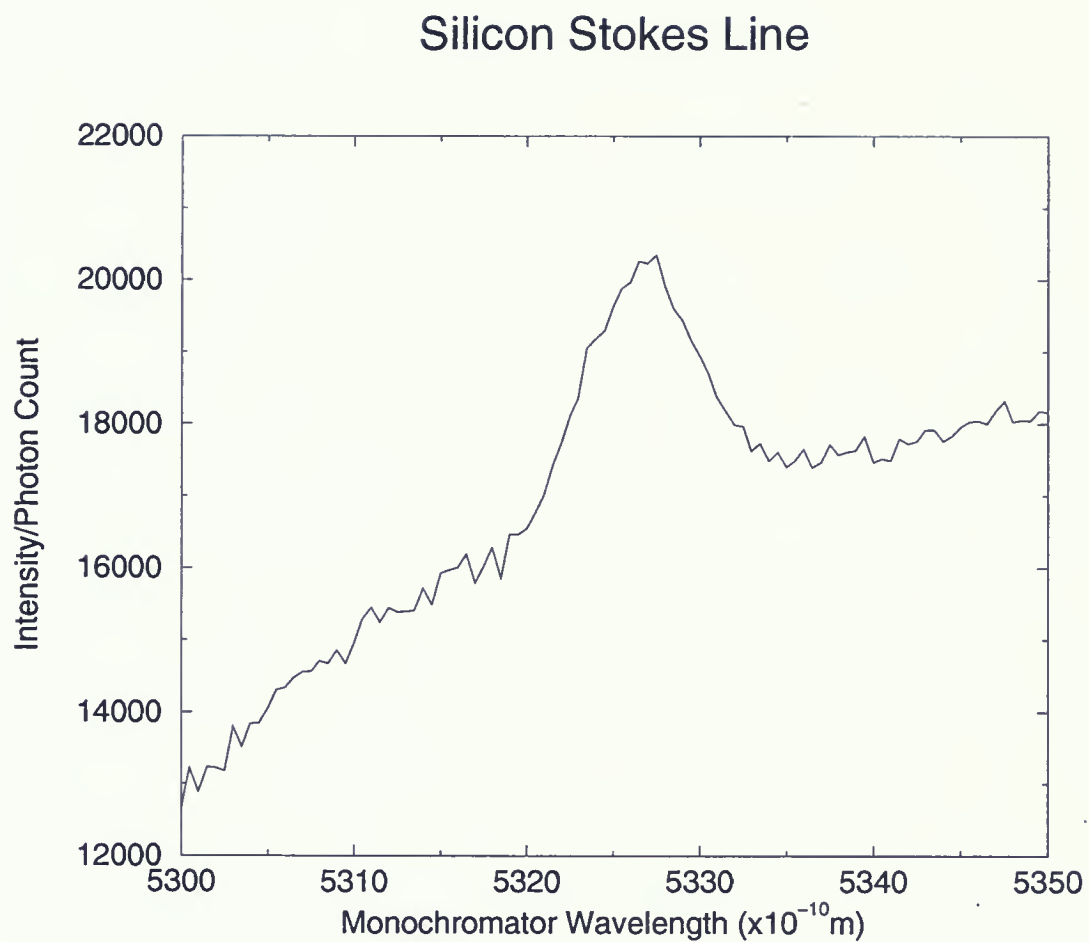
5.3 Software Settings

Overall, significant progress was made in regards to characterising the collection settings. Typical scan parameters were set to the values given in Table 5.2 below. Scans using these

Collection Parameter	Typical Setting
CMI	0.10s
MSD	1.00s
DWG	2.20s
PWT	2.55s
R/S	25

Table 5.2: Typical Collection Parameter Settings.

parameters showed a significant improvement over the first Silicon stokes run, Figure 4.6, mainly due to the increased wait time per wavelength point. The first Silicon scan taken with the settings outlined in Table 5.2 is presented in Figure 5.4, showing the improved silicon phonon mode sitting on a rising baseline. It was thought that the rising effect could be related to thermal stability of the detector or some type of electronic settling period. Chapter 6 describes the course of action taken to eliminate this trend.

Silicon Stokes Line

Figure 5.4: Rising effect: Electronics related? 63.75 s sampling time per point (2.55s, 25 readings).

Chapter 6

Need for Thermal Stability: Peltier Cooling

Following the work completed on optimising the detection software settings, attention was then turned to maximizing the quality of silicon stokes spectra and then adding the ability to subtract a dark count or background which is also included in each scan.

The dark count can be measured in two ways. Some systems incorporate a shutter that measures the dark count (detector only, no illumination) following the full intensity measurement at the same wavelength. This alternating procedure continues until essentially two measurements are taken at each wavelength yielding two (2) Intensity vs. Frequency power spectra; one representing the background or dark count and one representing the combined signal, which includes any structure present. Alternatively, a complete scan can be taken separately for each of the background and overall intensity. In this case, it is beneficial to complete the two scans as temporally close as possible; thus, reducing any possible influence from changes that can occur from one scan to the next. The latter procedure was employed for the work reported here.

During initial work it became evident that a problem existed with the power spectra measured to date. An overall rising structure was noted in the spectrum as wavelength (and time) increased. This was shown previously in Figure 5.4. In scanning for the Silicon stokes line one expects to find a flat baseline supporting a sole peak, such as that found in [3]. Clearly in Figure 5.4, this is not the case. In fact when another background scan was taken directly following a silicon stokes scan under the same conditions the background was found to be of higher intensity than the silicon stokes peak and baseline, as seen in Figure 6.1. Initially it was thought that there was simply some kind of
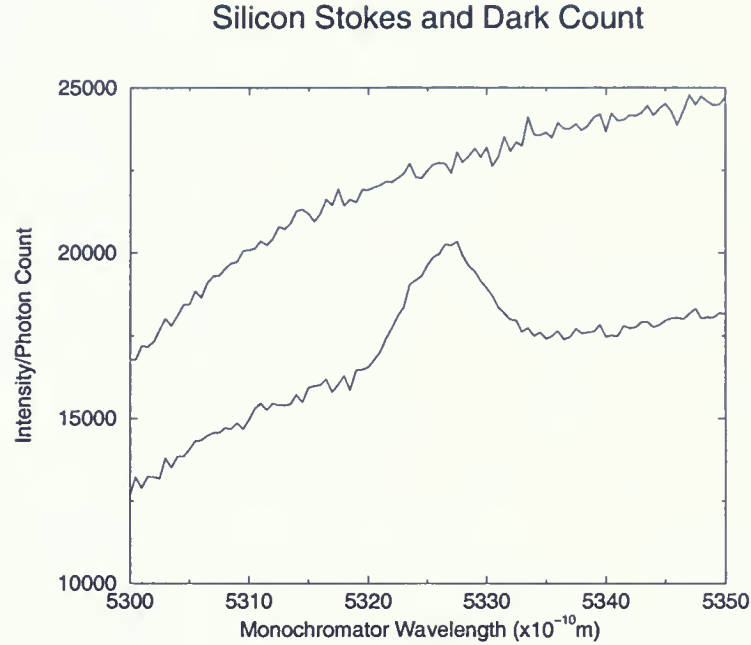
Figure 6.1: Silicon Stokes scan showing darkcount of higher intensity. 63.75s sampling time per data point.

lag or settling period associated with the detection electronics, as this had been noted in other systems in the past [28]. Thus, to test this, background scans were taken at three different intervals spanning over 22 hours. These results are presented in Figure 6.2 and seem to indicate a settling period that is somewhere in the region of 3 to 22 hours or higher. Although it seemed very long to wait before the detector was stable, a stokes scan and background were taken following a 22 hour wait. The results are shown in Figure 6.3. Notice the extremely high background. Another scan taken at a different position on the crystal face, under similar conditions is shown in Figure 6.4. It was thought that perhaps the previous position on the Silicon face was promoting more elastically scattered (laser) light into the monochromator, hence higher overall counts. Now the second scan shows a non-linear baseline and a rising background scan. Clearly, thermal stability and/or sensitivity of the detection electronics had now become another issue that had to be addressed, since these two scans performed under similar conditions showed that results were non-reproducible. Cooling the detector would imply control

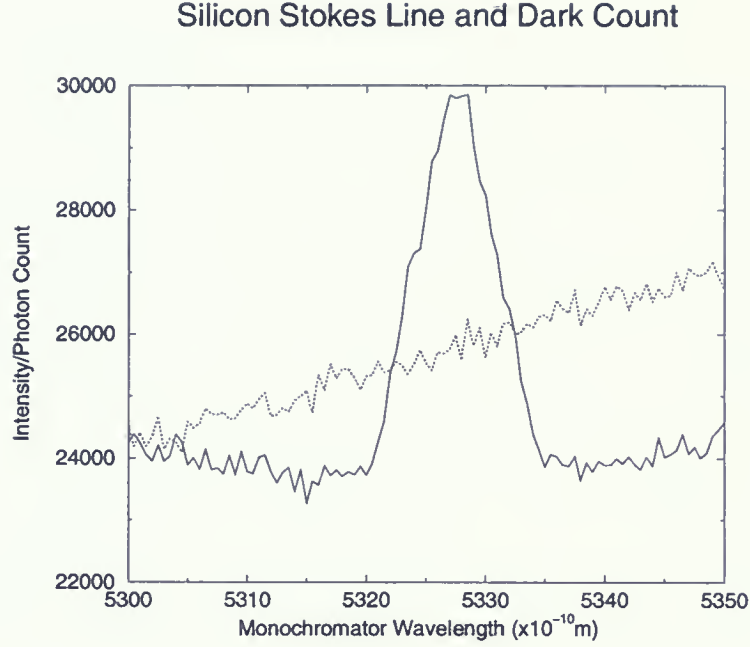**Dark Count of Detector**

effect of wait time to stabilization
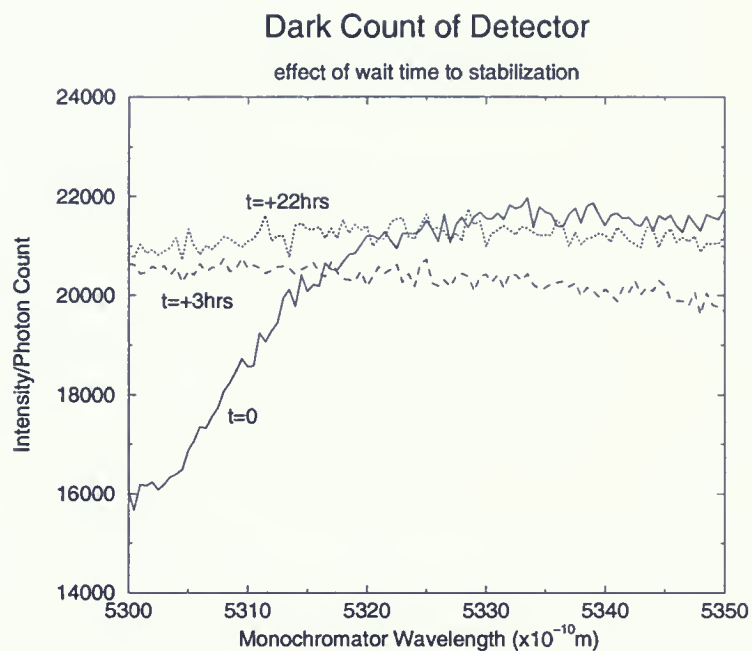
Figure 6.2: Warming/electronic stabilising effect over 22 hours. 63.75s sampling time per data point.

Silicon Stokes Line and Dark Count

detector on +22hrs 15mins
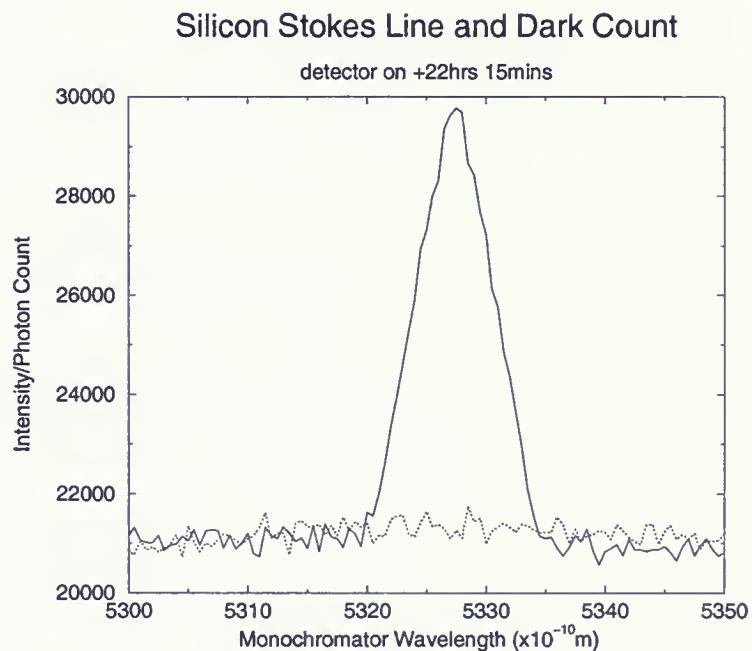
Figure 6.3: Stokes scan after 22 hours of waiting. 63.75s sampling time per data point.

Silicon Stokes Line and Dark Count

Figure 6.4: Stokes scan on new crystal face position. 63.75s sampling time per data
point.

over any thermal instability since the temperature of the detector and electronics could

be actively regulated. It also gives the added advantages of providing a slight increase

in sensitivity and lowering the dark count. For this model (*Electron Tubes P 10232*) the

Quantum Efficiency and consequently, sensitivity is a function of temperature, as shown

below. For every drop in ^oC, the detector gains some efficiency.

$$Q.E.\ gain = +(0.06 \rightarrow 0.08)\frac{\%}{^oC} \cdot (^oC\ Drop), \qquad (6.1)$$

for the Bi-Alkali photomultiplier operating at 5145 Å, giving a 3.3 % - 4.4 % (assuming an

operating temperature of -55°C) increase in efficiency over the 18 % discussed in section

3.3. The background or dark count also drops to a minimum of $\approx$ 10 - 32 counts per

second at 0°C or below. [16] The improvements following implementation of the cooling

system are clearly evident and are presented in the next section.

6.1   Spectral Improvement

Detector cooling is provided with an *in-house* produced Peltier attachment. This is a simple solid state device that allows heat to be pumped across an array (wall) of semi-conductor cells surrounding the detector. Heat is pumped in the direction of current flow and for the arrangement used in this work, a water jacket flowing around the solid state cooling elements provided an improved heat sink for the detector or heat source. A typical temperature gradient across the source and sink is approximately -60°C [29]. Consequently, depending on the temperature of the cold water supplying the jacket, the detector could easily be cooled to more than -55°C.

The system used a cooling dial setting (0-10) which varied the amount of current passing through the solid state device. More current flow implied more heat could be pumped away from the detector and that lower temperatures could be reached. The actual temperature near the detector is found by measuring the resistance across a platinum reference coil and comparing this to a standard value. At 0°C the resistance is measured as 100 Ω and each subsequent drop in temperature correlates to a unit drop in resistance. 1°C = 0.385 Ω. For example, a resistance measurement of 92.3 Ω implies the detector temperature is approximately -20 °C [6].

The first Silicon Stokes spectrum and background was taken with the cooling dial set at 4.47/10.00. The result is shown in Figure 6.5. A number of key differences are noted. First, the sensitivity has increased significantly as evident by the ratio of peak (max) to background. In fact, using *xmgr*, graphing software, the ratio of peak to background is calculated as approximately 3.7266. Secondly, the background scan is essentially flat within the noise, across the entire range as would be expected over a small range of wavelengths.
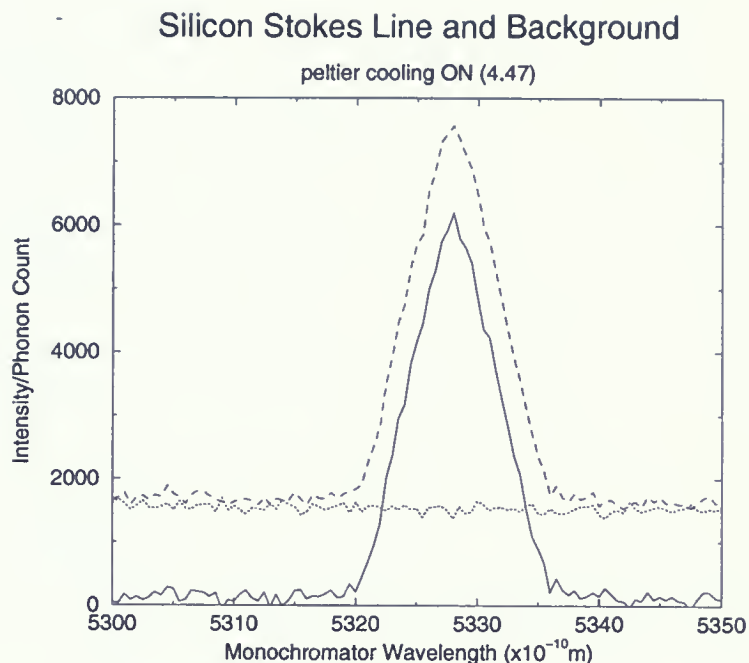
Figure 6.5: Silicon Stokes spectrum; cooling set at 4.47 ($\approx$ -39.2 °C). Solid line shows darkcount subtracted from combined signal. 63.75s collection time per point.

The next step was to find the best working temperature ranges for the detector since its sensitivity is a function of temperature, which is in turn a function of current applied (cooling dial setting). Some select results are summarized in Table 6.1. From Table 6.1,

COOLING DIAL	PEAK/BACKGROUND	RESISTANCE Ω	TEMPERATURE °C
3.50	3.5583	75.2	-64.4
4.00	3.1555	77.1	-59.5
4.13	3.4738	79.3	-53.8
4.20	5.4670	80.3	-51.2
4.25	4.8184	81.4	-48.3
4.47	3.7266	84.9	-39.2
4.60	2.4434	87.3	-33.0

Table 6.1: Peltier Cooling Settings for Peak/Background Ratio.

we see that the best working range is somewhere between -48°C and -53°C, or 4.25 and 4.13 on the cooling dial. A silicon stokes spectrum taken with the cooling set at 4.20 proved the best thus far and is shown in Figure 6.6.
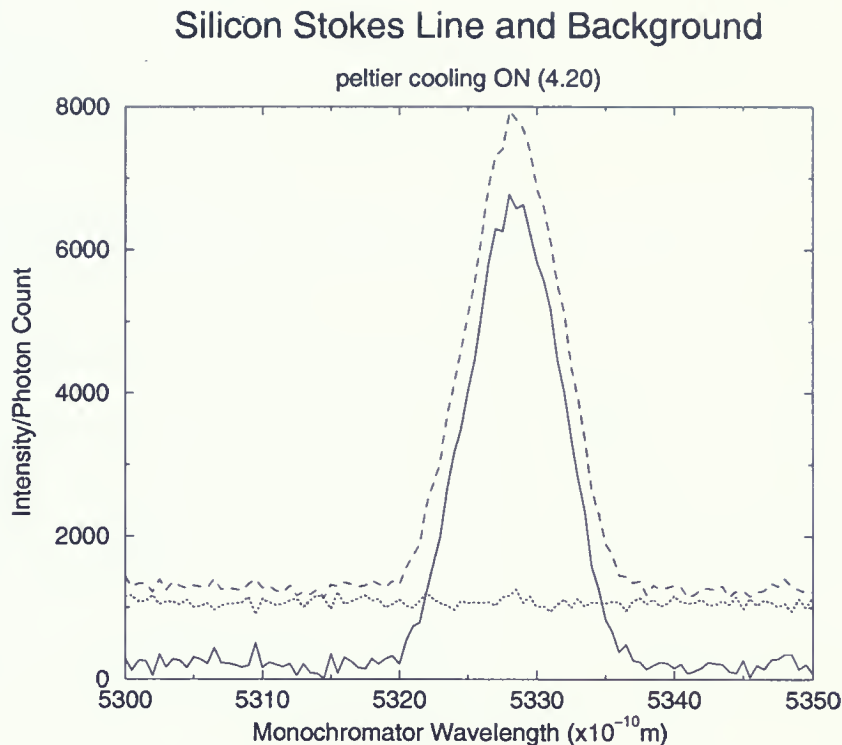
Figure 6.6: Silicon Stokes spectrum; cooling set at 4.20 ($\approx$ -51.2 °C). Solid curve shows darkcount subtracted from combined signal. 63.75s collection time per point.

The most important preliminary aspects of the system, such as;

- Calibration; Monochromator wavelength ($\mathring{A}$) vs. True wavelength ($\mathring{A}$).

- Collection settings optimisation

- Sensitivity and thermal stability of detector

had thus been established. The next goal was to improve resolution of the spectra prior to including the capability to carry out low temperature Raman spectra measurements (4K - 293K+) within the system.

Chapter 7

Slit Optimisation and Resolution

Prior to completing temperature dependent Silicon Stokes measurements, some work was carried out on optimising slit widths (narrowest exit possible) and gaining an understanding of their influence on the spectrum. The hope was to carry out temperature dependent Silicon Stokes measurements with high enough resolution that they could be readily compared with literature [3],[14], [25], [26].

7.1 Slit Trends

The intermediate slit was found to influence the spectral shape profoundly. Closing down this slit showed remarkable "selectional" ability. This trend is shown in Figure 7.1 (a), where the intermediate slit is varied from 1.5 mm - 3.5 mm. Closing the intermediate slit to less than 1.25 mm shows a significant reduction in signal strength, as presented in Figure 7.1 (b). Entrance and Exit slits were held constant and fairly wide at 2.5 mm each. The intermediate slit seems to be a major defining factor for determining the spectral band promoted through the spectrometer. Wide, flat peaks imply a "selection band" or "bandwidth" that is significantly broad with respect to the phonon mode or line itself. In such a case, as the selection band is moved across the scanning range there will be a number of points that report back the same approximate intensity. A selection band that is fairly narrow would select the points more discretely and give rise to a more well defined peak or spectral output, especially around the mode's (peak) centre. This is demonstrated in Figure 7.2. Intuitively, this selectional ability of the intermediate slit makes some sense, since light entering the monochromator is already diffracted once
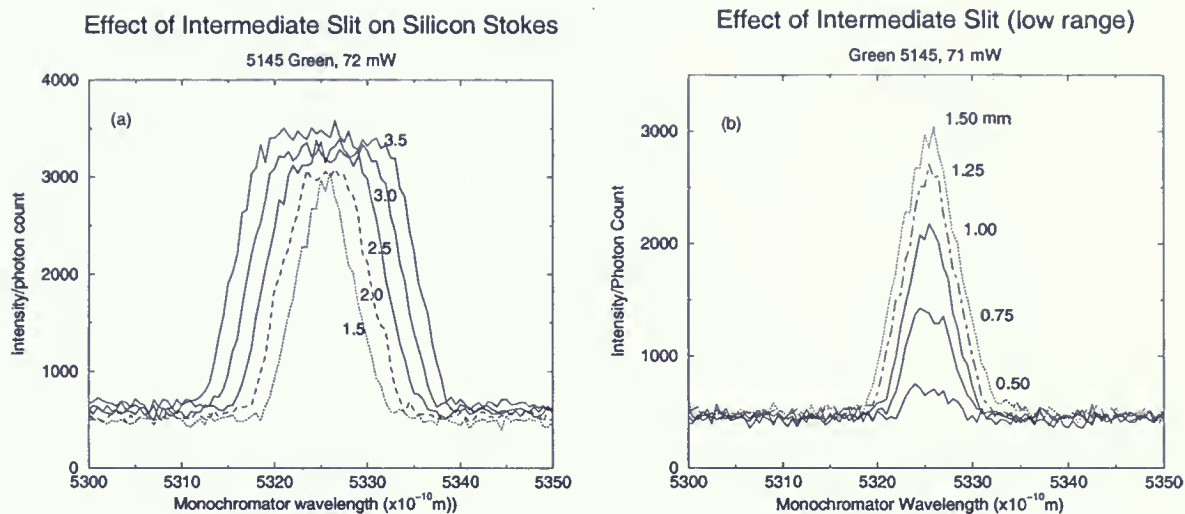
Figure 7.1: Effect of Intermediate Slit on Spectra. Entr., Exit = 2.5mm (25.0s sampling time per point).
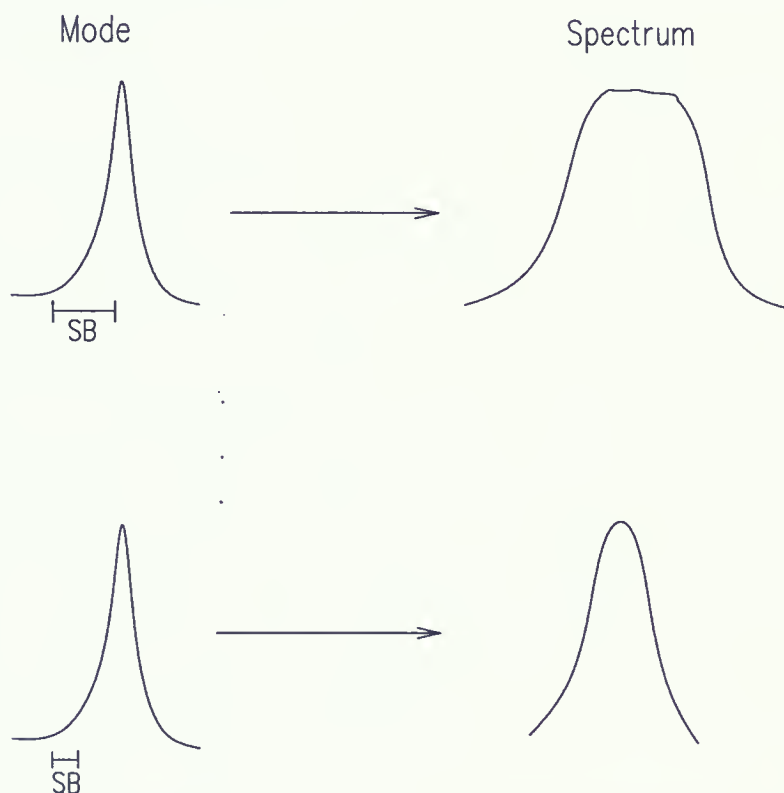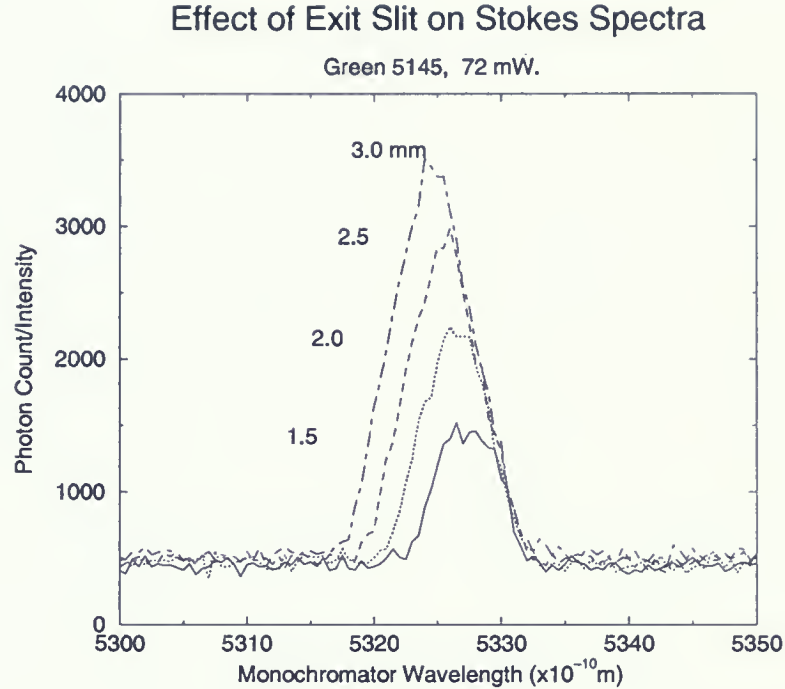

Figure 7.2: Consequence of Selection Band Size.

Figure 7.3: Exit slit trend. Entr., Inter. = 2.5 mm, 1.375 mm repectively. (25.0s sampling time per point).

before being directed toward the intermediate slit, where a small band is "selected" to pass into the second monochromator.

The trend of the exit and entrance slits also demonstrated some interesting behaviour. For example, referring to Figure 7.3 we see the effect of opening the exit slit successively wider. Notice the shift toward lower wavelengths of the peak centre and drastic increase in signal strength. The intermediate slit and entrance slits are fixed at 1.375 mm and 2.500 mm respectively. As the exit slit is opened in increments of 0.5 mm from 1.5 mm to 3.0 mm, it causes a ≈ 1.04 Å negative shift in wavelength of the peak centre. As can be expected the ratio of peak to background is increased, however the half-width only increases by a maximum of ≈ 0.05 Å. It was thought that the exit slit would have a much more dramatic effect on the spectral resolution or half width of spectra. [12] states that full intensity should be possible with slits as small as 10μm and from Figure 7.3 we clearly see a dramatic decrease in signal with the slits as large as 2.0 mm.

In contrast to the exit slit, the entrance slit shows a trend of shift in peak centre
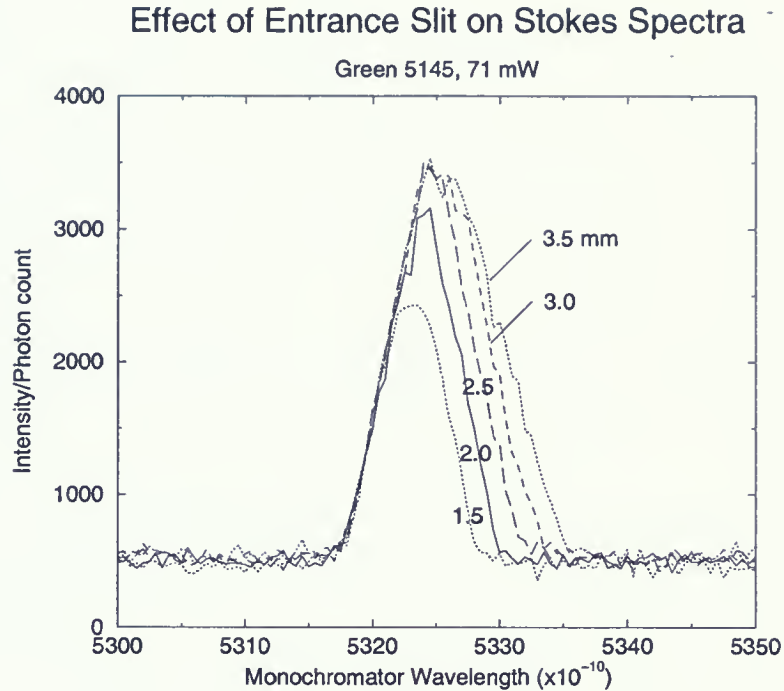
Figure 7.4: Entrance slit trend. Inter., Exit = 1.375, 3.0 mm respectively. (25.0s sampling time per point).

toward higher wavelengths or a positive shift, as it is opened successively. This is shown in Figure 7.4. The exit and entrance slits seem to have opposite effects on spectral output. In the case of the entrance slit a 0.5 mm increase in slit width causes a 0.30 - 0.89 Å positive shift in the peak centre (toward higher wavelengths). It also introduces some extra noise, assumed to be from the introduction of more ambient light or elastically scattered components into the first monochromator.

Considering the trends of the Entrance, Intermediate and Exit slits, if one were to set all slits to 1.5 mm for example, then from Figure 7.1, Figure 7.3 and Figure 7.4 we see that almost no signal would reach the detector. This is due mainly to the "cut-on" and "cut-off" features of the Exit and Entrance slits. In fact, a scan with the Entrance, Intermediate and Exit slits set at 2.5 mm, 3.5 mm and 1.0 (or lower) respectively, showed no visible phonon peak at all. The evidence presented here suggests that a re-alignment of the spectrometer will need to be undertaken if high resolution spectra are to be obtained. However, due to time constraints it could unfortunately not be undertaken, particularly

since it was advised that the procedure was extremely time-consuming (see sub-section 3.1.1). Thus, it was decided to proceed with obtaining temperature dependent measurements to demonstrate the cryostats viability, even though it was known that the spectral resolution of these scans would be below literature standard.

7.2 Optimised Silicon Stokes Peak

Immediately prior to beginning temperature dependent runs a final spectrum was obtained with what were decided as the best settings. The selection criteria used to obtain the best slit settings was based on Figure 7.1, Figure 7.3 and Figure 7.4 and other work completed on attempting to characterise the influence of the various slits. Ideally, the best settings would provide a great deal of sensitivity or High ratio of peak to background (Ratio in Table 7.1) and a narrow FWHM (good resolution). Table 7.1 below summarizes these results taken directly from each plot without any mathematical fitting. Table

Exit (mm)	Entrance (mm)	Intermediate (mm)	Ratio	FWHM Å
1.900	1.900	1.375	2.8910	6.26
2.000	2.000	1.375	3.7841	6.29
2.125	2.000	1.375	3.8342	6.36
2.250	2.000	1.375	4.1522	6.40
2.375	2.000	1.375	4.7658	6.37
2.500	2.000	1.375	5.0615	6.36
2.500	2.125	1.375	5.4285	6.14
2.500	2.250	1.375	5.8241	6.29
3.000	2.250	1.375	6.2887	6.78
3.000	2.500	1.375	6.5966	7.46

Table 7.1: Effects of Slits on Intensity and FWHM.

7.1 presents the optimum (narrowest) FWHM achieved in this work as ≈ 6.14 Å which corresponds to a measurement of ≈ 21.65 cm^{-1}, whereas literature [14] reports a value of 4.16 cm^{-1}. The final silicon spectra taken at Room temperature (293 K) with the best slit settings is displayed in Figure 7.5 in Å and in Figure 7.6 in cm^{-1}. The FWHM

Silicon Stokes 1st TO Phonon Mode

Green 5145, 86 mW
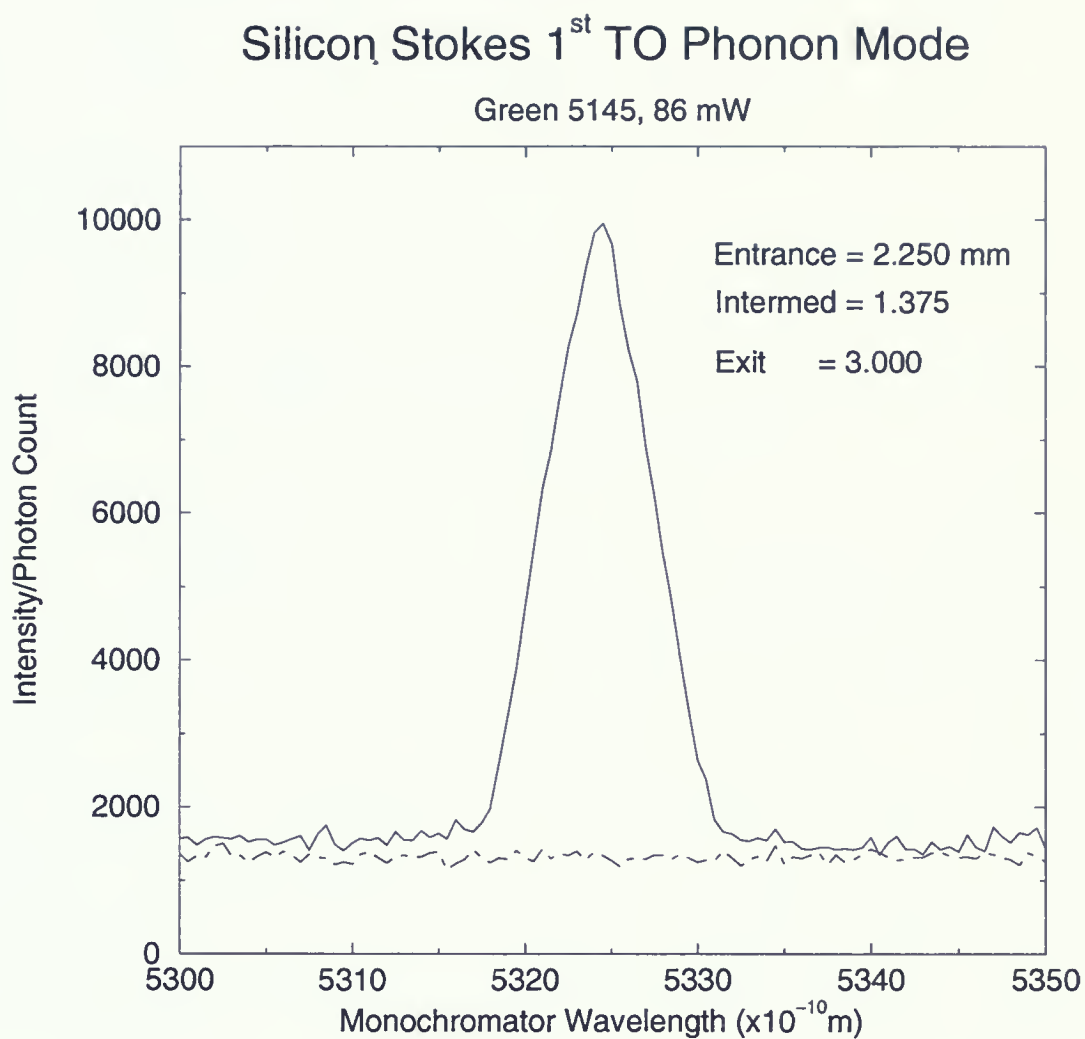
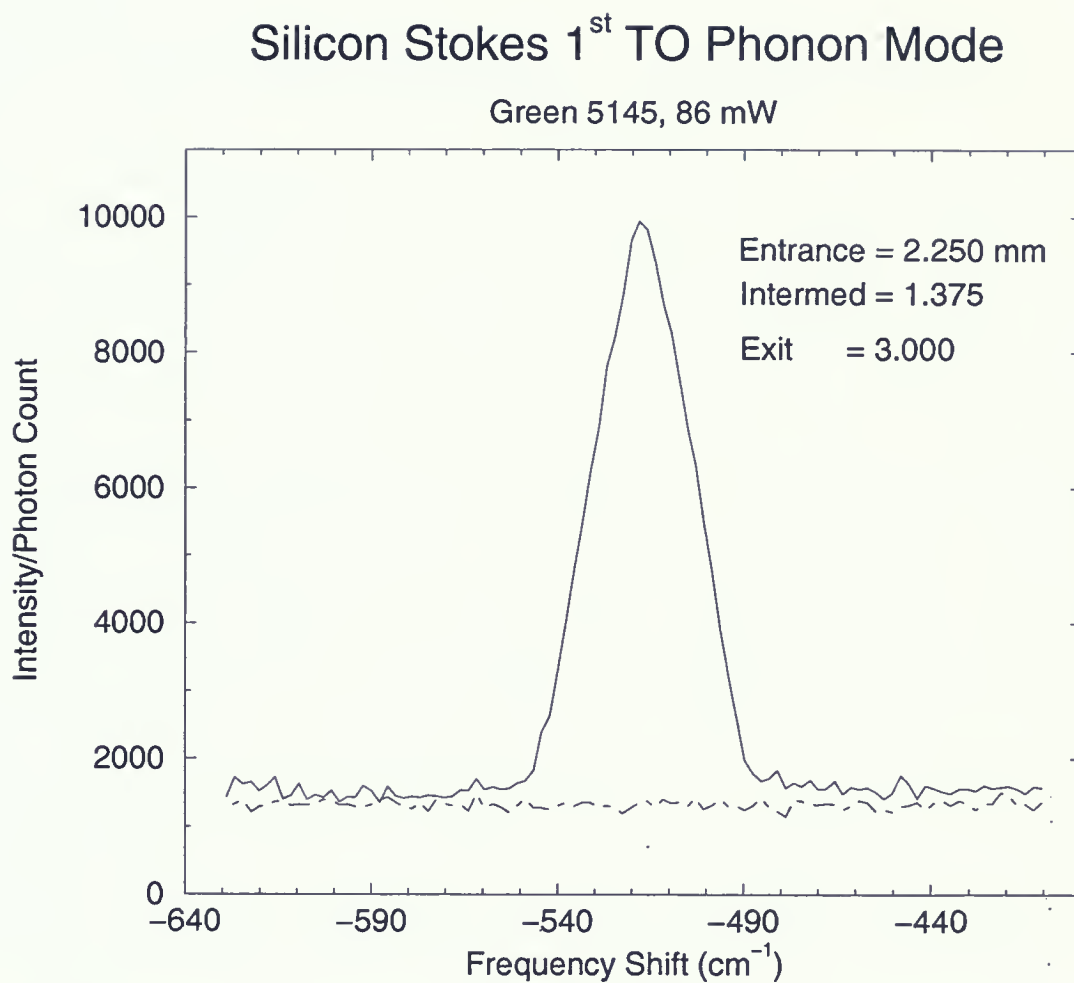**Figure 7.5:** Best silicon spectra to date. 76.5s sampling time per point (2.55s, 30 readings).

for this spectrum is 6.78 Å or 23.91 cm^{-1}. It was decided that a slightly higher FWHM would be compensated by the larger ratio of peak to background, as presented in Table 7.1.

Figure 7.6: Best silicon spectra to date. Showing Shift from Laser. 76.5s sampling time per point (2.55s, 30 readings).

Chapter 8

Silicon Stokes Temperature Dependent Data and Analysis

Figure 8.1 shows silicon stokes spectra taken at a variety of temperatures. The 4K spectrum was measured first, followed by warming to intermediate temperatures of 77K and 150K. The 293K room temperature spectrum was taken last, after leaving the system to warm up overnight. The upward shift of the background is thought to be caused by an ice film or similar layer forming over the surface of the silicon sample. This may indicate that even with vacuum pressures on the order of 10^{-6} torr, it is not sufficient to prevent moisture or gases present in the cryostat chamber from collecting and freezing on the sample face. This could be remedied by warming up to room temperature between measurements (note that the 293K and 4K curve are not affected by this problem) or by switching to a UHV (10^{-9} - 10^{-10} torr) arrangement. At this level any residual particles present should be at a negligible level. In fact, [28] had noticed this behaviour in previous Raman low temperature experimental work. In Figure 8.2 the additional background is subtracted. Although the resolution is very low, a mathematical fit was performed on the temperature dependent data in order to examine whether any influence of the decreasing temperature could be observed. The poor resolution, however, resulted in peaks that are much more "triangular" than "Lorentzian" and thus, the fits were relatively poor. The fit results are given in Table 8.1. The fitting program, *REFCAL* could only approximate the peak centres to the nearest $\mathring{A}$, whereas it actually varies from ≈ 5325.3 to ≈ 5326.2. Table 8.1 lists the actual peak centre positions, as opposed to those found by REFCAL, since they are more representative of the actual position.
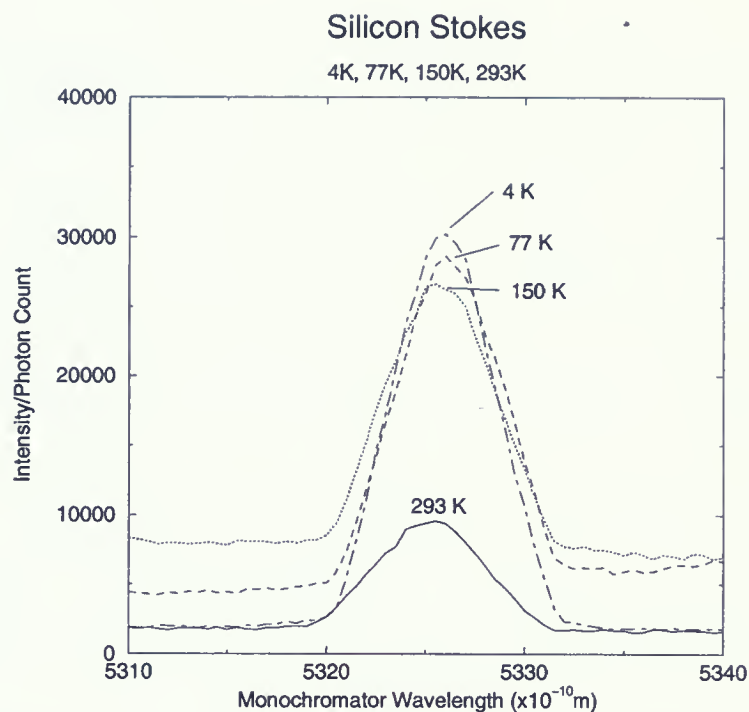
Figure 8.1: Silicon Stokes Temperature Dependent Data (76.5s sampling time per point).
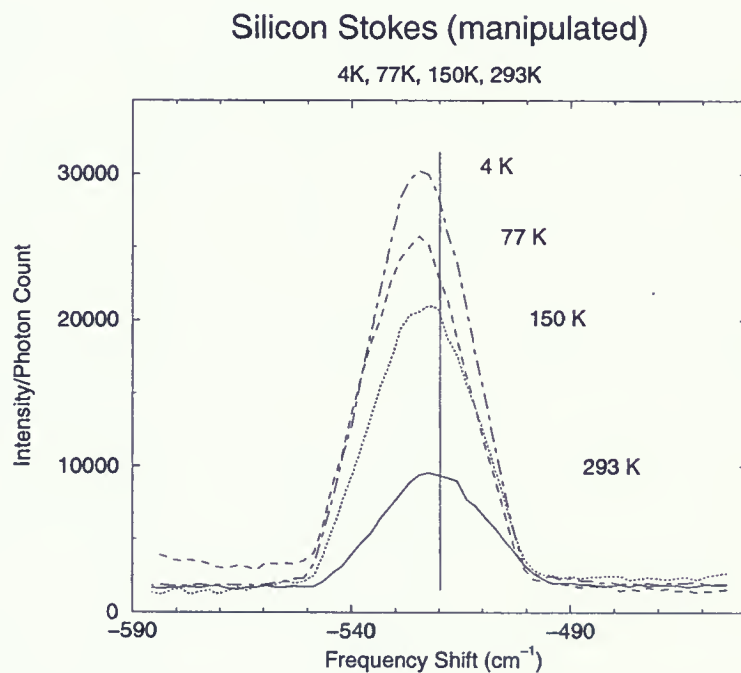
Figure 8.2: Silicon Stokes Temperature Dependent Data (manipulated).

Temperature (K)	Peak Centre (True cm^{-1})	FWHM (cm^{-1})	Freq. Shift (cm^{-1})	Peak Intensity (arb.)
4	18 912	23	-525	29 596
77	18 911	26	-525	28 916
150	18 913	25	-524	25 740
293	18 915	25	-521	16 397

Table 8.1: FWHM and Intensity Fitting Parameters for Silicon from REFCAL Lorentzian Fit. Actual peak centres used for shift calculation before being rounded.

Work done by [3] using data taken at temperatures ranging from 20K to 770K, indicates that the Silicon phonon mode undergoes three pronounced changes as temperature is decreased over this range; namely, a negative frequency (cm^{-1}) shift (hardening) of $\approx$ 2.6 % (or $\approx$ 0.70 % from 20K to 300K), a narrowing of the phonon mode (FWHM) by $\approx$ 67 % and an increase in intensity or photon count of roughly 50 %. In this thesis, Silicon Stokes Raman spectra were obtained at 4K, 77K, 150K and 293K. Over this range, Table 8.1 shows that there is a slight negative shift in frequency (0.687 %) as temperature is decreased and that the behaviour of the FWHM also seems to correlate somewhat with literature, showing a small decrease(8.96 %). The peak intensity of the phonon mode shows a significant increase as temperature is decreased (80.5 %) from 293K to 4K, also correlating with literature trends. Since changes in sample geometry likely occur upon cooling, a comparison of absolute intensities as temperature decreases is excluded.

Given that the spectra were obtained with such poor resolution, making an absolute comparison of the linewidth with literature values impossible, there is surprisingly good agreement between the frequency shift of the stokes line versus temperature and those of [3]. Figure 8.3 shows a comparison of the results of this work with [3]. Note that in both cases the frequency shift at liquid Helium temperature is less than the value at liquid Nitrogen temperature. [3] Suggests that this may be related to the minimum in the Debeye temperature of Silicon which occurs near 40K. The fact that, in spite of the poor

resolution we were able to detect this small effect shows the accuracy of the calibration of the system and suggests that once the resolution problem has been resolved, research grade Raman spectra will be obtained with this system.

The absolute error associated with the temperature dependent frequency shift is estimated to be on the order of $\pm$ 2-3 cm^{-1}, since the resolution problem makes it extremely difficult to pinpoint the Stokes peak shift with any reasonable accuracy. For example, in section 4.1 the shift is found to be 518.11 cm^{-1} with an exit slit width of 3.00 mm, however, in Table 8.1 the Stokes shift is found to be 521.10 cm^{-1} (or $\approx$ 521 cm^{-1}) with an exit slit width of 2.50 mm. The relative error under similar experimental conditions is estimated to be on the order of 0.3% and is included in Figure 8.3.

In the work produced here, well defined spectra were only obtained with the exit slit set at 2.5 mm or higher, which is much wider than the 10 μm suggested by the monochromator manual [12] and also wider than the 30 μm slit used by [3]. A significant reduction in the operational slit sizes would provide much higher resolution in Raman spectra and consequently, allow peak centres and the FWHM to be measured with greater accuracy and be compared with literature values.

Silicon Stokes Frequency Shift vs. Temperature

comparison to literature
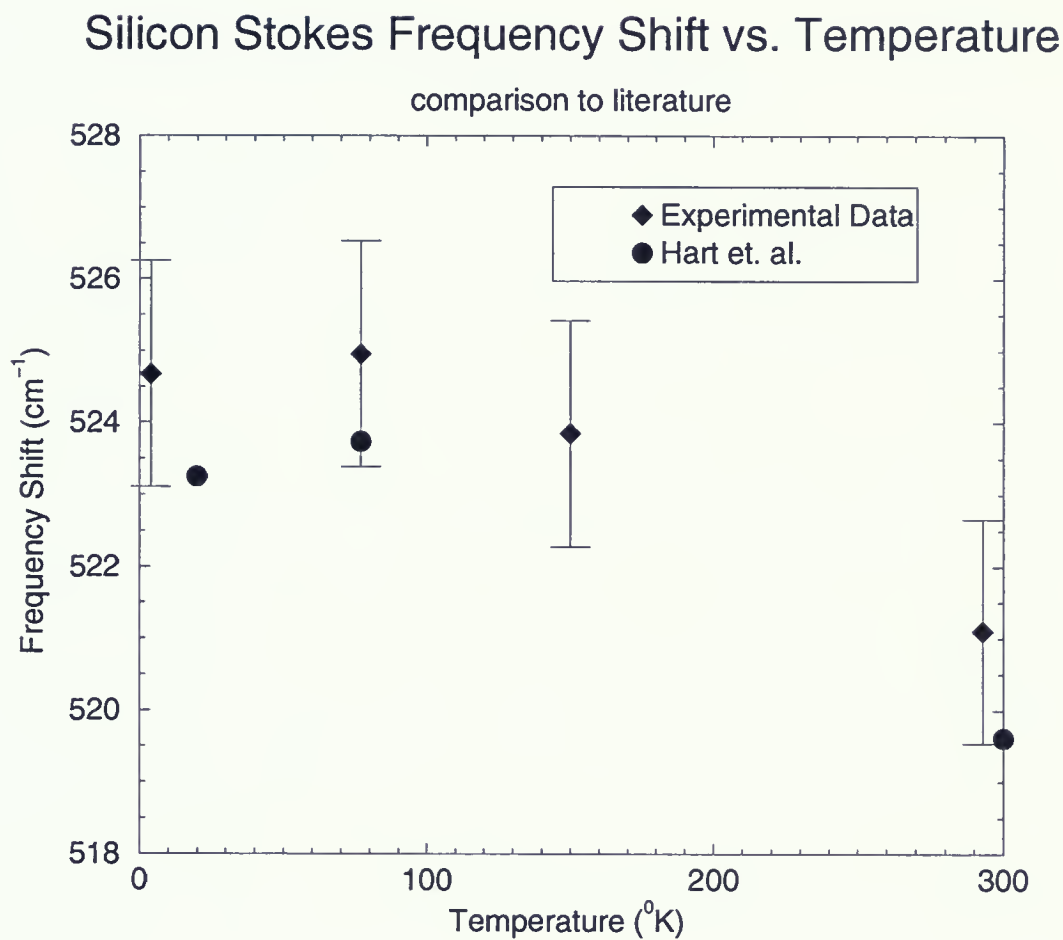
Figure 8.3: Temperature Dependence of Silicon Stokes Frequency shift compared to Literature [3]. Relative error shown.

Chapter 9

Conclusions and Future Considerations

Overall the project was successful in moving toward a research grade system, capable of measuring accurate temperature dependent Raman spectra. This is shown by the significant progress made in;

- updating the collection optics to include a cryostat,

- calibrating the double monochromator output to within 1-2 cm^{-1} of literature values,

- and optimisation and characterisation of the slits, the Peltier cooling unit, and the software collection parameters.

While significant improvement in overall spectral quality and reproducibility was achieved over the course of this work, due to time constraints, several procedures which are crucial and/or highly desirable for obtaining research grade spectra remain to be addressed by future users of the system.

The greatest hurdle to overcome lies in the form of the proposed spectrometer re-alignment. All evidence discussed in chapter 7 suggests that successful completion of this procedure would yield significant improvement in spectral resolution. If in fact, this can be reduced to 2 - 4 cm^{-1} [3], [14], temperature dependent Raman scattering measurements of new materials can be carried out.

Assuming the re-alignment is undertaken, one may also consider the replacement of the existing gratings, if this were a viable option at that time. It was noted by [13] that the

gratings were "dull and grey" in appearance, thereby inhibiting full intensity throughput.

Further improvement can be achieved through a change of detectors and/or incident wavelength. In the Green range (5145 $\mathring{A}$) the Bi-Alkali photomultiplier only operates with $\approx$ 18 % efficiency. This increases to $\approx$ 25 % in the Blue (4880 $\mathring{A}$) region [16]. There are other detectors commercially available that would give a much larger output and are significantly more efficient in either the Green or Blue range [28].

Lastly, cylindrical focusing optics as suggested by [3] would serve to improve the focus of the scattered image on the entrance slit. This would be a fairly significant improvement over the traditional spherical optics employed presently to focus/capture the scattered radiation from the sample in question. This is because the laser or incident radiation glances across the surface of the silicon (or other sample) and thus, the spherical optics focus an oval or "elongated" image on the entrance slit. Ideally a finely focused, small "dot" would give the best results.

If any one of these changes could be implemented it would certainly improve the existing system. However, as it stands the arrangement exhibits significant potential as a research apparatus for Vibrational Spectroscopy.

Appendix A

Plasma Line Literature Values and Data

As outlined in section 4.1, plasma emission lines were compared to literature [1] by obtaining a good quality plasma line scan over a given range and then superimposing their positions on the literature values. To identify the literature values with those obtained in the plasma line scans, one first had to calibrate the plasma lines obtained by using a previous, rough calibration found by [2] or [6] and then attempting to identify the possible emission lines tabulated in the literature. The process was essentially cyclic, since as more lines were identified a more accurate calibration could be found. This calibration could be used to re-calibrate and identify more emission lines, which yielded a more accurate calibration equation etc.

Emission lines were identified to the left (wavelength) of the laser line and to the right. Referring to Figure 4.3, we see that the monochromator was calibrated over a 643 $\mathring{A}$ range. The 43-point calibration equation given in Table 4.2 was typically accurate to 1-2 cm^{-1}. The 43-point calibration implied, forty three emission lines were identified in plasma line scans; 20 were found to the left of the laser line (Figure A.1) and 23 were found to the right of the laser line (Figure A.2).

Some lines are easily identified from Figure A.1 and Figure A.2, however, many of the emission lines are of low relative intensity and hence, difficult to view in a scale which shows all lines. Therefore, all lines that were identified are given in Table A.1 for reference.
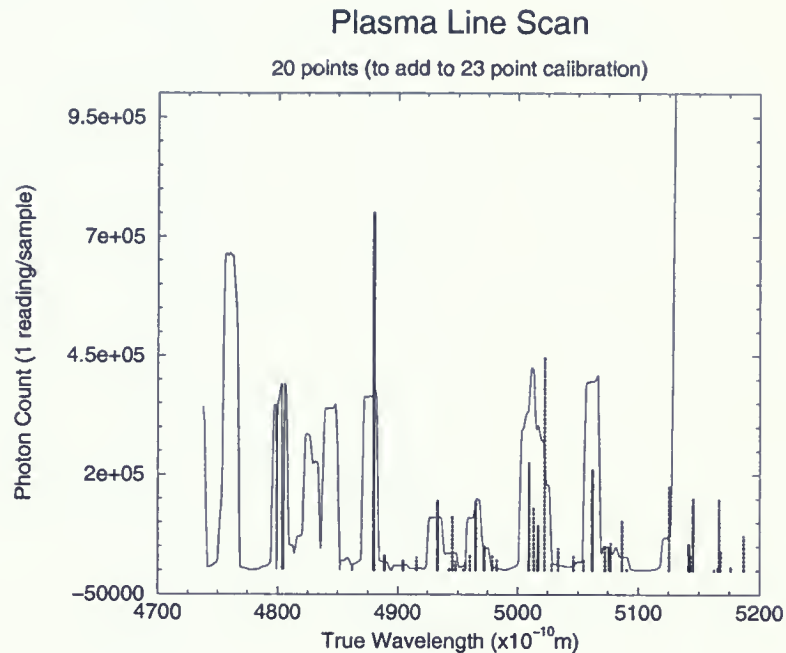
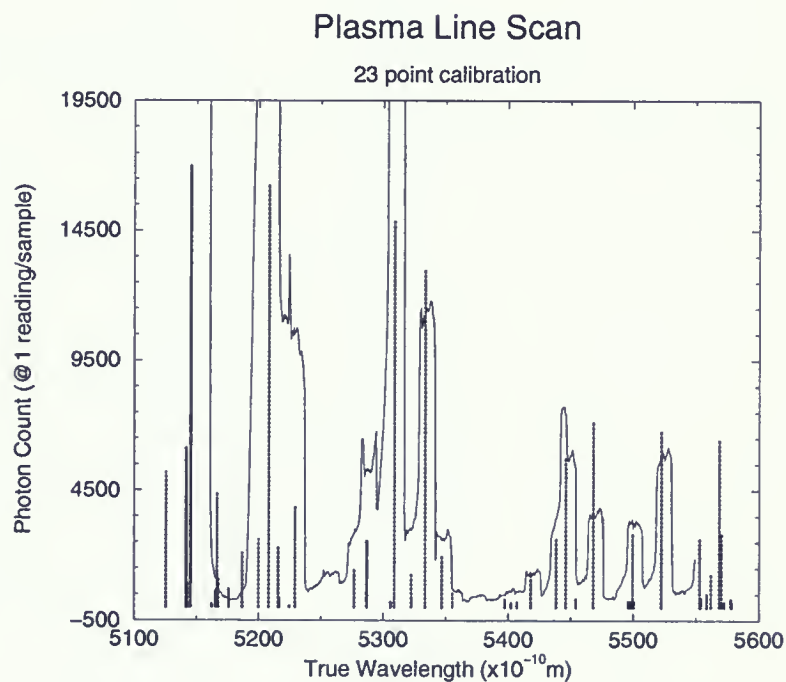**Figure A.1:** Plasma and literature lines to left of Laser, 5145 Å.

Figure A.2: Plasma and literature lines to Right of Laser, 5145 Å.

True Wave. (Å)	Monoch. Wave. (Å)	Line Type (Ar/Kr)
4879.860	4988.74	Ar
4889.033	4998.77	Ar
4904.753	5011.30	Ar
4915.9	5022.58	Kr
4933.206	5033.44	Ar
4945.6	5045.13	Kr
4965.073	5062.26	Ar
4972.157	5068.53	Ar
4978.9	5074.37	Kr
4982.8	5078.97	Kr
5009.334	5094.84	Ar
5013.3	5099.44	Kr
5017.160	5104.45	Ar
5022.4	5110.30	Kr
5062.036	5139.95	Ar
5072.5	5149.98	Kr
5077.2	5153.74	Kr
5086.5	5162.09	Kr
5090.496	5167.94	Ar
5125.7	5190.91	Kr
5187.0	5243.43	Kr
5208.3	5259.48	Kr
5216.0	5267.51	Kr
5216.816	5270.19	Ar
5224.9	5273.54	Kr
5229.5	5277.55	Kr
5276.5	5317.03	Kr
5286.895	5325.73	Ar
5308.7	5343.79	Kr
5322.8	5357.18	Kr
5333.4	5364.54	Kr
5346.8	5372.57	Kr
5355.5	5378.59	Kr
5397.522	5416.73	Ar
5402.604	5420.74	Ar
5407.348	5425.43	Ar
5418.4	5434.13	Kr
5438.6	5448.18	Kr
5446.3	5454.20	Kr
5454.307	5459.55	Ar
5468.2	5475.61	Kr
5499.5	5499.70	Kr
5522.9	5519.10	Kr

Table A.1: All literature plasma emission lines identified and used in calibration.

Bibliography

[1] C. Julien and C. Hirlimann. Calibration of a Raman Spectrometer Using the Kr^+ Laser Plasma Lines. *J. Raman Spec.*, 9:62, 1980.

[2] M. Janssen. Raman Scattering Program. B.Sc. thesis, Brock University, 2001.

[3] T. R. Hart, R. L. Aggarwal and Benjamin Lax. Temperature Dependence of Raman Scattering in Silicon. *Phys. Rev. B*, 1:638, 1970.

[4] K.O.S.I. Comparison of Infrared and Raman Spectroscopies. Raman Rxn Systems, Raman Products Technical Note: Publication No. 1102, Kaiser Optical Systems Inc., 2003.

[5] Herman A. Szymanski, editor. *Raman Spectroscopy: Theory and Practice*. Plenum Press, NewYork, 1967.

[6] Tyler Kerr. NSERC USRA work term: Final report. Brock University, 2000.

[7] C. V. Raman. A New Radiation. *Indian J. Physics.*, 2:628, 1928.

[8] K.O.S.I. Raman Spectroscopy - An Overview. Raman Rxn Systems, Raman Products Technical Note: Publication No. 1101, Kaiser Optical Systems Inc., 2003.

[9] Stanley K. Freeman. *Applications of Laser Raman Spectroscopy*. John Wiley & Sons, Toronto, 1974.

[10] Charles Kittel. *Introduction to Solid State Physics. 7th ed.* John Wiley & Sons Inc., Toronto, 1996.

[11] Scott Kirkby. Chemistry 444/455 web-notes. www.umr.edu/~pchem/spec/pdf/ spec.lecture14.winter2002.pdf, University of Missouri-Rolla, 2002.

[12] Jarrel-Ash Co. 1.0 m Double Czerny-Turner Scanning Spectrometer. User manual, engineering publication no. 25-100, Jarrel-Ash Co., 1967.

[13] Dr. R. Hackl. Private communication. Brock University, 2002.

[14] J. H. Parker Jr., D. W. Feldman and M. Ashkin. Raman Scattering by Silicon and Germanium. *Phys. Rev. B*, 155:712, 1967.

[15] Klaus Betzler. Grating Spectrometer. Lecture Summary Notes. Fachbereich Physik, Universitat Osnabruck. www.home.uos.de/kbetzler/notes/, 2002.

[16] Detector Modules Group. P10232 Series of Photodetector. User manual, CR Instruments Inc., 2000.

[17] Dr. A. Van Der Est. Private communication. Brock University, 2002.

[18] D. Reznik. Electronic Light Scattering in Layered Cuprates. Ph. D. Thesis, University of Illinois at Urbana-Champaign, 1993.

[19] UIUC. UIUC Advanced Physics Laboratories: Phys3p71 web-notes. www.wug.physics.uiuc.edu /courses/phys371/371exp/d7/d7.pdf, Physics Dept., University of Illinois at Urbana-Champaign, 2000.

[20] Advanced Products Department. Model LT-3-110 Liquid Transfer Heli-Tran Refrigerators. Operating manual, Air Products and Chemicals Inc., 1973.

[21] Oriel Ins. # 52660 Bandpass Filter. Product Data Sheet, Oriel Instruments, 1999.

[22] K.O.S.I. Holographic Notch and Super Notch Filters. Product Spec. Sheet/Manual, Kaiser Optical Systems Inc., 2001.

[23] H. Tang and I. P. Herman. Raman mircroprobe scattering of solid silicon and Germanium at the melting temperature. *Phys. Rev. B.*, 43, 1991.

[24] K.O.S.I. Raman Calibration Accessory Protocol. Raman Rxn Systems, Raman Products Technical Note: Publication No. 1300, Kaiser Optical Systems Inc., 2003.

[25] Paul A. Temple and C. E. Hathaway. Multiphonon Raman Spectrum of Silicon. *Phys. Rev. B.*, 7:3685, 1973.

[26] A. Zwick and R. Carles. Multiple-order Raman Scattering in Crystalline and Amorphous Silicon. *Phys. Rev. B*, 48:6024, 1993.

[27] L. A. Kuzik, V. A. Yakovlev, and G. Mattei. Raman Scattering enhancement in Porous Silicon Microcavity. *Applied Phys. Lett.*, 75:1830, 1999.

[28] Dr. M. Reedyk. Private communication. Brock University, 2003.

[29] Electronics Shop. Private communication. Brock University, 2004.